# Vorticity Structures behind Wing Tips

**Pavel Anderle**

# Vorticity Structures behind Wing Tips

by

**Pavel Anderle**

**Thesis submitted to the University of Glasgow**
**Department of Aerospace Engineering**
**for the degree of Master of Science**
**March 2005**

**The research was supported by BAE SYSTEMS**

# Acknowledgements

The work described in this dissertation was carried out by the author whilst a full-time student at the Aerospace Engineering Department at the University of Glasgow during the period October 2001 to October 2002.

The author wishes to acknowledge the support of the academic and technical staff of the Aerospace Engineering Department, especially the excellent advice and encouragement given by his supervisors, Dr. Ing. L. Smrček and Prof. F. N. Coton, during the course of his work.

Special thanks go to the technical staff of the Spencer Street Laboratory, especially to Mr. R. Gilmour who helped with the experimental set-up and to Mr. T. Smedley, Mr. A.Erwin, Mr. J. Kitching and Mr. A. Fraser for their help in manufacturing and installing the equipment. It was a pleasure to work with them and the other employees of the Spencer Street Laboratory.

I would also like to thank Prof. Brož for his help in analysing the experimental data.

I am grateful to Mr. Polmesil and to the Hph company for the manufacturing of the wing-tip models.

The financial support of BAE Systems also is gratefully acknowledged.

# Summary

This thesis describes an experimental investigation of the velocity and vorticity distributions in the flow field behind wing-tip devices.

During the experimental programme, four types of full size wing-tips from the sailplanes were investigated experimentally. Effort was focused on gaining a greater understanding of how the wing-tip geometry modifies the vortex structure behind the wing.

The research involved examining the velocity and vorticity distribution in the flow field, using hot-wire anemometry. In order to carry out measurements with the hot-wire anemometry system, a new traverse mechanism was designed, manufactured and set-up. This traverse mechanism was integrated with the other test instrumentation to create a complete measurement chain. The complete system allows fully automated hot wire measurements to be made over a defined area using programmable test parameters. The measurements were performed in the Handley-Page wind tunnel of the Aerospace Engineering Department at the University of Glasgow.

Firstly, the flow field behind a G-304 sailplane's standard wing-tip was measured to determine the vorticity structure and wing tip vortex location. The next step of the project was to test two versions of the G-304 sailplane's winglet and one wing-tip extension to clarify the effect these have on the vorticity structure and downwash distribution.

The flow fields behind the wing tip models were measured in three planes at different angles of attack. For all tests the free stream velocity was set at 33 m/s (118.8 Km/h) which corresponds to a Reynolds number of Re = 0.8 $x10^6$ based on the mean chord of the main wing. Data analyses and graphical presentations were carried out using Tecplot software in the form of vector plots of velocity distribution and contour line plots of the vorticity component.

The results illustrate the effectiveness of the system in capturing the differences in the flow structures behind the various wing tip devices.

They also highlight the role of the different wing tip slopes in modifying the wing induced flow field. This allows conclusions to be drawn in terms of the contribution of winglet to the total circulation and to the induced drag.

# Contents

**Acknowledgements** ..... i

**Summary** ..... ii

**Contents** ..... iv

**List of Figures** ..... vi

**List of Tables** ..... xi

**Nomenclature** ..... xii

**Chapter1. Introduction** ..... 1

1.1 Induced Drag and Wing-tip Vortex Formation ..... 2

1.2 Winglets for Sailplanes ..... 6

1.3 Aim of the Project..... ..... 10

**Chapter 2. Test Facilities** ..... ..... 11

2.1 Wind Tunnel ..... 11

2.2 Wind Tunnel Test Configuration ..... 13

2.2.1 Measurement Procedure ..... 13

2.2.2 Traverse Mechanism ..... 14

2.2.3 Hot Wire Anemometry ..... 16

2.2.4 Investigation Grid ..... 19

2.2.5 Wind Tunnel Models of Winglets..... 20

**Chapter 3. Experimental Results** .....23

**3.1 Results I:** Wing Tip Model A ..... 24

3.1.1 Observations ..... 24

3.1.2 Vector Plots of Velocity Distribution and Contour Plots of Vorticity distribution ..... 26

3.1.3 Downstream Wake Position ..... .....29

**3.2 Results II:** Winglet Model B .....30

3.2.1 Observations ..... 30

3.2.2 Vector Plots of Velocity Distribution and Contour Plots of Vorticity distribution ..... 32

3.2.3 Downstream Wake Position .....35

**3.3 Results III:** Winglet Model C .....36

3.3.1 Observations ..... 36

3.3.2 Vector Plots of Velocity Distribution and Contour Plots of Vorticity distribution ..... 38

3.3.3 Downstream Wake Position ..... 42

**3.4 Results IV:** Wing Tip Model D ..... 43

3.4.1 Observations ..... 43

3.4.2 Vector Plots of Velocity Distribution and Contour Plots of Vorticity distribution ..... 44

3.4.3 Downstream Wake Position ..... 47

**Chapter 4. Analysis of the Results** .....48

**4.1** Circulation: Definition and its Relation to Vorticity ..... 48

**4.2** Numerical Analysis of the Vorticity Distribution in terms of Circulation ..... 53

**4.3** The Discussion of Experimental Results ..... 62

**Chapter 5. Conclusions** ..... 72

**Appendix**

Hot Wire Anemometry and the Concept of Effective Velocity .....74

**References** .....82

# List of Figures


Figure 1: Drag vs. speed ..... 3

Figure 2: Drag coefficient and lift coefficient vs. aspect ratio ..... 4

Figure 3: Inwash, outwash and vortices development ..... 5

Figure 4: Lift distribution over low and high wing aspect ratio ..... 7

Figure 5: Winglet thrust ..... 8

Figure 6: Wind tunnel test-section ..... 11

Figure 7: Handley Page wind tunnel circuit ..... 12

Figure 8: Wind tunnel test configuration ..... 13

Figure 9: Wind tunnel testing section and winglet model position ..... 14

Figure 10: Traverse mechanism ..... 15

Figure 11: Winglet models (1:1) placed in Handley Page wind tunnel ..... 16

Figure 12: CTA bridge ..... 17

Figure 13: X-wire sensor Dantec 55P51 ..... 17

Figure 14: Flow chart of data acquisition ..... 18

Figure 15: Investigation grid ..... 19

Figure 16: Key design parameters of winglets ..... 20

Figure 17: Sailplane HpH 304 CZ, 304C Wasp ..... 21

Figure 18: Wind tunnel wing tip models ..... 22

Figure 19: Velocity and vorticity distribution behind wing tip model A, angle of attack 0 degrees ..... 26

Figure 20: Velocity and vorticity distribution behind wing tip model A, angle of attack 3 degrees ..... 27

Figure 21: Velocity and vorticity distribution behind wing tip model A, angle of attack 6 degrees..... 28

Figure 22: Downstream wake behind wing tip model A ..... 29

Figure 23: Velocity and vorticity distribution behind winglet model B, angle of attack 0 degrees ..... 32

Figure 24: Velocity and vorticity distribution behind winglet model B, angle of attack 3 degrees..... 33

Figure 25: Velocity and vorticity distribution behind winglet model B, angle of attack 6 degrees..... 34

Figure 26: Downstream wake behind winglet model B ..... 35

Figure 27: Velocity and vorticity distribution behind winglet model C, angle of attack 0 degrees ..... 38

Figure 28: Velocity and vorticity distribution behind winglet model C, angle of attack 3 degrees..... 39

Figure 29: Velocity and vorticity distribution behind winglet model C, angle of attack 6 degrees..... 40

Figure 30: Velocity and vorticity distribution behind winglet model C, angle of attack 9 degrees..... 41

Figure 31: Downstream wake behind winglet model C ..... 42

Figure 32: Velocity and vorticity distribution behind wing tip model D, angle of attack 0 degrees ..... 44

Figure 33: Velocity and vorticity distribution behind wing tip model D, angle of attack 3 degrees..... 45

Figure 34: Velocity and vorticity distribution behind wing tip model D, angle of attack 6 degrees..... 46

Figure 35: Downstream wake behind wing tip model D ..... 47

Figure 36: Coordinate system and velocity components definition ..... 50

Figure 37: Definition of Circulation in the plane YZ behind wing tip models .... 50

Figure 38: Vorticity area enclosed by the closed curve C ..... 51

Figure 39: General function .....52

Figure 40: Definition of integration paths – model A ..... 54

Figure 41: Definition of integration paths – model B ..... 56

Figure 42: Definition of integration paths – model C ..... 58

Figure 43: Definition of integration paths – model D ..... 60

Figure 44: Circulation behind wing tip model A ..... 65

Figure 45: Circulation behind winglet model B .....66

Figure 46: Circulation behind winglet model C .....67

Figure 47: Circulation behind wing tip model D ..... 68

Figure 48: Summary of circulation behind wing tip models .....69

Figure 49: Downstream wake position
behind wing tip model A vs. winglet model B ..... 70

Figure 50: Downstream wake position
behind winglet model C vs. wing tip model D ..... 71

Figure 51: X-wire sensor Dantec 55P51 ..... 75

Figure 52: Illustration of the effective velocity ..... 75

Figure 53: Probe positions and yaw angle calibration of the X-wire sensor .....79

Figure 54: Data table – voltage vs. velocity .....80

Figure 55: The x-wire sensor specific calibration curves ..... 80

Figure 56: The yaw angle calibration table ..... 81

# List of Tables


Table 1: Technical data of HpH 304CZ, 304C Wasp sailplane ..... 21

Table 2: Dependence of the circulation magnitude on integration path for wing tip model A ..... 55

Table 3: Dependence of the circulation magnitude on integration path for winglet model B ..... 57

Table 4: Dependence of the circulation magnitude on integration path for winglet model C ..... 59

Table 5: Dependence of the circulation magnitude on integration path for wing tip model D ..... 61

# Nomenclature

| | |
|---|---|
| AR | aspect ratio, $b^2/S$ |
| b | wing span |
| c | chord length |
| $C_{Di}$ | induced drag coefficient |
| $C_D$ | total drag coefficient |
| $C_L$ | wing lift coefficient |
| Re | Reynolds number |
| U | free stream velocity |
| u,v,w | local velocity components in (x,y,z) direction respectively |
| $u_\theta$ | azimuthal velocity, cylindrical coordinates |
| y,z | cross-stream coordinates |

Greek Characters

| | |
|---|---|
| $\alpha$ | wing angle of attack |
| $\Gamma$ | circulation |
| $\omega$ | vorticity |
| $\lambda$ | taper ratio, $c_{tip}/c_{root}$ |

# Chapter 1

## 1. Introduction

In the late 1960s, designers began experimenting with 'small' vertical extensions on wing tips to reduce the formation of tip vortices. The winglet concept actually dates back to 1897, when Frederick Lanchester took out a patent on the idea, incorporating it into some of his wing theories (Lanchester, 1907). His wing had two 'capping planes' at the end of it, that became known in the 1920s as 'end plates', when Prandtl extended his basic lifting line concept (Prandtl, 1920). Lanchester and Prandtl had been working on similar theories but they had difficulties communicating with each other (Jupp, 2001). Independently they established the classical model of trailing vorticity behind a wing today known as 'Lanchester-Prandtl theory'.

The initial effort on winglets started at NASA in the 1960s. The procedures how to manage such wing arrangements were presented at NASA. (Blackwell, 1969). The real break-through in winglets was made by Whitcomb. In 1976, Richard Whitcomb, a NASA aerodynamicist, published a paper that compared a wing with a winglet and the same wing with a simple extension to increase its span. Whitcomb showed that winglets reduced drag by about 20 percent and increased the wing lift-drag ratio by approximately 9 percent. Induced drag represents about 30 percent of the total drag of a transport plane at cruise condition, so the induced drag reduction has a significant effect on fuel consumption. Whitcomb began a focused investigation into winglet aerodynamics and tested several designs in the wind tunnels at the NASA Langley Research Center (Whitcomb, 1976).

The first industry application of the winglet concept appeared on general aviation passenger jets. For instance, it has been claimed that a winglet on a B-747 can significantly reduce fuel consumption on long-range flights. Research into the effect of winglets on first generation jet transport wings showed that they can produce reasonable drag reduction at high lift conditions (Montoya, 1977), (Fell).

Winglets are now being incorporated into most new commercial aircrafts such as the Boeing and Airbus transport jets. Airbus has added winglets to the A310, A300-600, A318/319/320/321 (except the A320-100), A340 and the A380 to improve wing aerodynamic efficiency. The A300 and A310 established Airbus as a major competitor to Boeing and allowed the company to go ahead with the more ambitious A330/A340 family. Since the 1980s, most high performance sailplanes also have vertical wing tip extensions.

## 1.1 Induced Drag and Wing tip Vortex Formation

Airplanes have three primary sources of drag (Figure 1). The first part comprises the basic airfoil and parasite drag, the second is induced drag or drag due to lift and the third source is caused by compressibility effects. The parasite drag relates to the increased skin friction and form drag arising from the interference effect of airplane parts. For sailplanes, compressibility drag is not an issue. The induced drag is a significant contributor to the total drag at high angles of attack and is a result of generating lift on a finite wing.

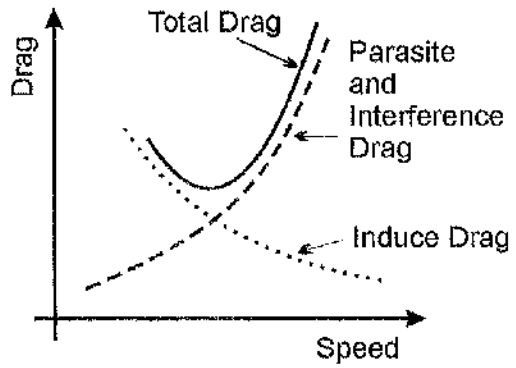


Figure 1. Drag vs. speed

Literature suggests that the percentage of induced drag is about 70% of the total drag during climb, 25% during cruise and 40% during landing (Volkers, 1996). It is therefore feasible to try to reduce the induced drag as a means of improving the aircraft performance. It is generally assumed that the induced drag is independent of the viscous drag, so it is calculated for a non-viscous fluid (Eppler, 1995). The total drag coefficient is composed of two parts, the zero lift drag and the induced drag. The induced drag is often written in a coefficient form as:

$$C_{D_i} = \frac{C_L^2}{\pi \cdot AR \cdot e} \tag{1}$$

where $C_L$ is the aeroplane lift coefficient and $AR$ is the wing aspect ratio. High aspect ratio wings have lower induced drag than short, thick, low aspect ratio wings (Figure 2). In addition, the wing platform shape also affects the induced drag. The parameter $e$, called the efficiency factor or Oswald's factor, is a function of the aeroplane geometry and configuration. It is equal to 1.0 for an elliptic lift distribution on a wing and is less than 1.0 for any other aeroplane configuration.

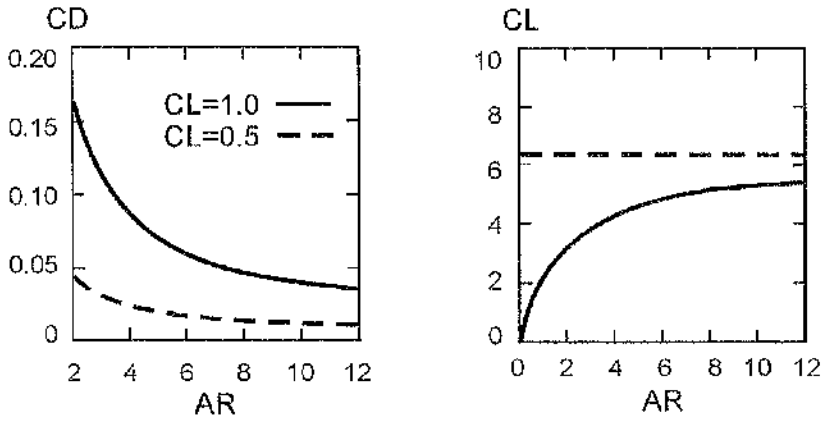


Figure 2. Drag coefficient and lift coefficient vs. aspect ratio

Generally, the shape of a wing is designed such that the flow particles have to travel longer distances along the upper surface of the wing than along the lower surface, when the wing passes through the air. Due to this, the dynamic pressure is greater above the wing than under it and consequently the static pressure is lower above the wing than under the wing. This pressure essentially generates the lift required.

This pressure difference gives rise to a secondary flow at the wing tip. Air tends to flow from an area of high pressure to areas of lower pressure. The effect of this secondary flow is a deflection of the free stream, called outwash on the lower surface and inwash on the upper surface. This deflection of the air stream caused by the pressure difference combined with the forward movement of the plane produces a wingtip vortex (Figure 3). The vortex contains energy in the form of a swirling flow.

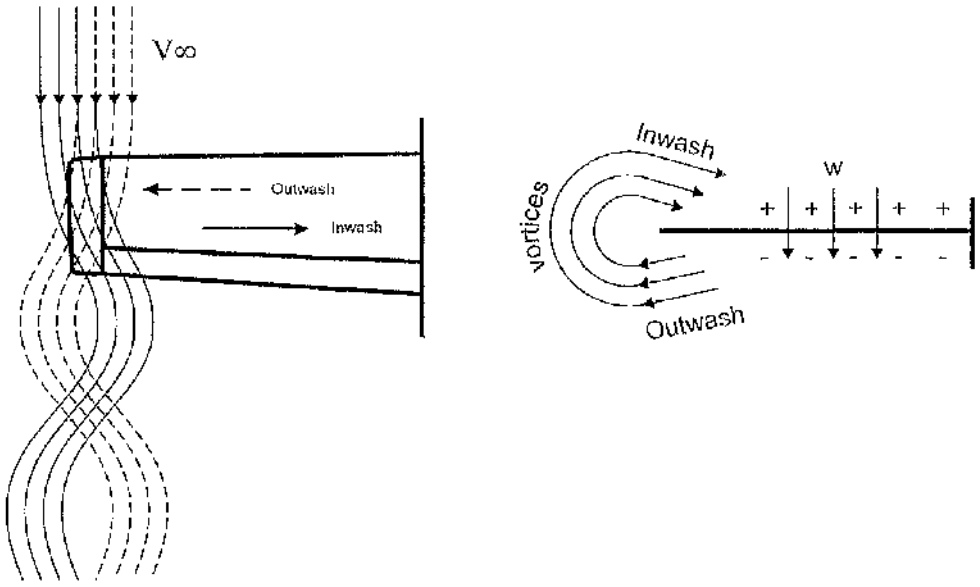


Figure 3. Inwash, outwash and vortices development

The wing tip vortices on large aircraft can be so powerful as to endanger smaller aircraft flying behind them. The energy in the vortices can be modified through displacement or reduction. These modifications can be further categorized as active and passive devices (Jarvis, 1999).

Active devices are devices added to the wing tips which incorporate moving parts. One of these ideas is the wing tip turbine (Patterson, 1991). Wing tip propellers have also been proposed as a method to reduce induced drag (Snyder, 1968).

Passive devices have fixed geometries and work to sustain the high pressure on the bottom of the wing and the low pressure on the top of the wing whilst modifying the tip vortex structure. Wing tip modifications such as the cut wing tip or drooped wing tip modify the vortex by simply changing the tip geometry. These modifications

change the location of the vortex core. In this way, the effective span of a wing can be increased, reducing the induced drag.

Basic modifications to wing tips can be achieved through the addition of surfaces such as end plates. A more efficient approach, however, is the Whitcomb winglet which takes advantage of twist to get a component of the winglet's lift in the thrust direction. Another example of this type of approach is the wing tip sail (Allen, 1976), (La Roche, 1996).

## 1.2 Winglets for Sailplanes

Different classes of airplanes have different requirements. A fighter aircraft has a low wing aspect ratio in order to suppress compressibility effects and moreover to acquire acceptable manoeuvrability. Conversely low fuel consumption is one of the main requirements for transport planes during cruise. In comparison, sailplanes require an efficient wing design in order to remain aloft for as long as possible.

Theory and experience have shown that the most efficient sailplane wing is one that is very long and slender. Having a high aspect ratio wing (2) is one way of cutting wing-tip losses. In essence, the longer wing has the same tip losses but those energy losses will affect a lesser proportion of the total wing (Figure 4). In other words, the lift is distributed over a longer wingspan and the trailing vorticity is spread out, dissipating less energy.

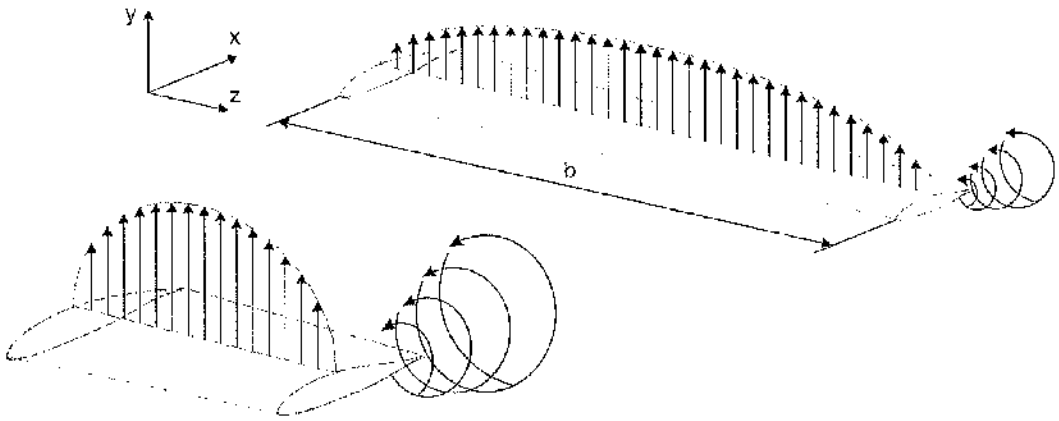


Figure 4. Lift distribution over low and high wing aspect ratio

Wing Aspect Ratio AR :

$$AR = b^2/S , \qquad \text{where } S \ldots \text{Wing Area} \qquad (2)$$

From a structural point of view, a long wing is prone to bend and has to be strengthened; this adds weight. The winglet provides the effect of an increased aspect ratio without extending the wing-span and so does not increase the wing root bending as much as an actual span extension would. The moment arm of the lift from a span extension is approximately 45% of the wing semi-span whereas the moment arm of winglet lift is roughly only one-half of the vertical winglet span. This small increase does not overload the wing or significantly alter the standard operating limitations. The addition of winglets on sailplane wings also improves the maximum lift/drag ratio, which is of importance for sailplanes under span-limited FAI requirements (Thorsen, 1999).

The first sailplanes to have winglets were the ASW-20FP, GEMINI and NIMBUS 3. Sets of Whitcomb style winglets were fitted to these wings in the late 1980's. Flight

tests carried out on these sailplanes demonstrated the effect of winglets on high aspect ratio wings (Marsden, 1991).

The primary effect of the winglet is to control the cross flow in the tip region of the wing in such a way as to reduce induced drag by displacing the vortices outward. The air flowing over the winglet, due to the presence of the tip vortex, strikes the winglet at an angle of attack. The winglet, like any wing, also produces lift which, in this case, has a component in the forward direction. Thus, the winglet produces thrust (Figure 5). This thrust component alters the cross flow at the wing tip and recovers some of the performance that would be lost through the additional drag caused by the increase in wetted area.

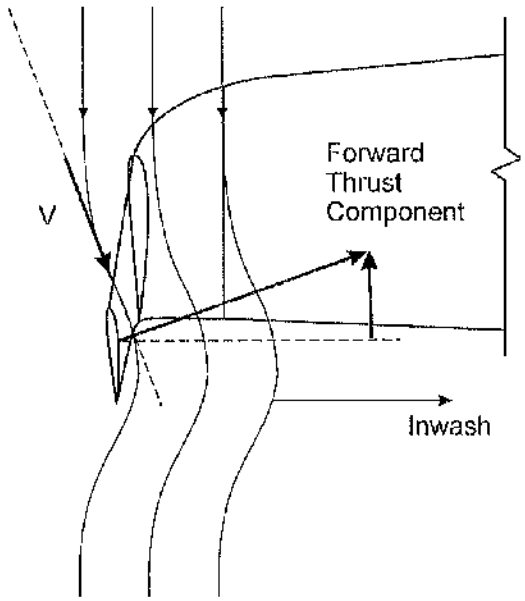


Figure 5. Winglet thrust

The induced drag coefficient is proportional to the square of the lift coefficient hence the reduction in drag also improves climbing capability (Nicks, 1983) (Nicks, 1993). This improvement can be used when sailplanes circle in thermal bubbles, the main

source of power to stay aloft (Kiceniuk, 2001). To have a maximum cross country speed during sailplane competitions is another important consideration. The induced drag benefit of winglets is greatest at higher lift coefficients and lower flight velocities, while the profile drag penalty grows in magnitude as the lift coefficient decreases and the velocity increases. Hence, the design of winglets must involve the compromise of maximizing the low speed improvement without sacrificing high-speed performance (Smith, 1997).

The winglet added to the ASW-19 sailplane clearly showed that for some speeds the friction drag could exceed the induced drag reduction provided by winglets (Masak, 1992). A correctly designed winglet can, however, be reasonably effective as illustrated in a study using the ASW-20 sailplane (Crosby, 1996).

The minimum induced drag depends on maximizing both the span and the span efficiency. The span efficiency usually decreases with increasing span. The lift distribution of a very high aspect ratio wing can be far from elliptical. As a result, the increase in span efficiency due to a properly designed winglet can cause a greater reduction in induced drag than a comparable span increase (Maughmer, 2001).

## 1.3 Aim of the Project

The aim of the project consists of three particular tasks which may be specified as follows:

1) Design and manufacture of a new experimental facility making possible measurements of velocity distributions past wing models in a wind tunnel.
   A particular feature of this facility was the traverse mechanism. This had to cover a region of the flow field large enough to capture the vortex systems of the models tested in the Handley Page wind tunnel. Moreover it had to reduce the acquisition time associated with previous traverse systems.

2) Verification of the operation of the experimental measurement system in terms of data validation, processing of the results and general reliability of the system.

3) Make introductory measurements to investigate the distribution of induced velocity downstream of the wing and to examine the effect of wing tip geometry on the wing vortex wake.

# Chapter 2

## 2. Test Facilities

The measurements were performed in the Handley Page wind tunnel, of the Department of Aerospace Engineering at the University of Glasgow, using hot wire anemometry. In order to carry out these measurements a new traverse system was designed and manufactured.

## 2.1 Wind Tunnel

The Handley Page wind tunnel is an atmospheric low-speed wind tunnel with a closed return circuit (Figure 7) equipped with a rectangular test-section of dimensions 2.15 m by 1.60 m and of length 3.38 m (Figure 6). The corners have 650 mm fillets that house lamps to provide lightings. Visual access to the working section is provided by 0.84 square meters of plate glass and acrylic windows that permit the model to be viewed from many angles. A turntable 0.97 meter in diameter, built into the test section floor can rotate models mounted on it. Several venting slots in the tunnel walls at the test section exit maintain near atmospheric static pressure.

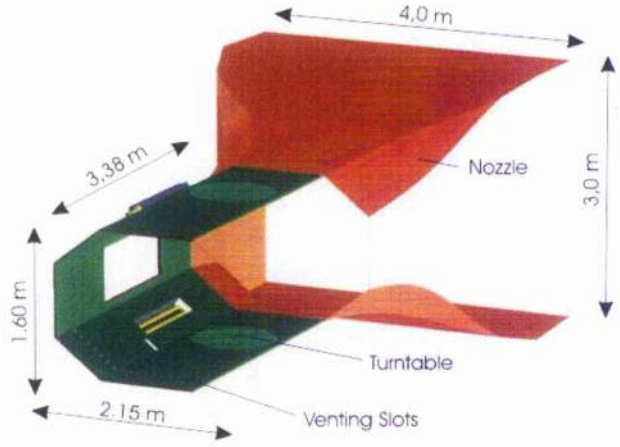


Figure 6. Wind tunnel test section

The nozzle ahead of the test section has a contraction ratio of 4:1. The power supply is an electric motor that drives a fan, 2.3 m in diameter, to provide the airflow in the wind tunnel. The tunnel can reach speeds up to 60 m/s.

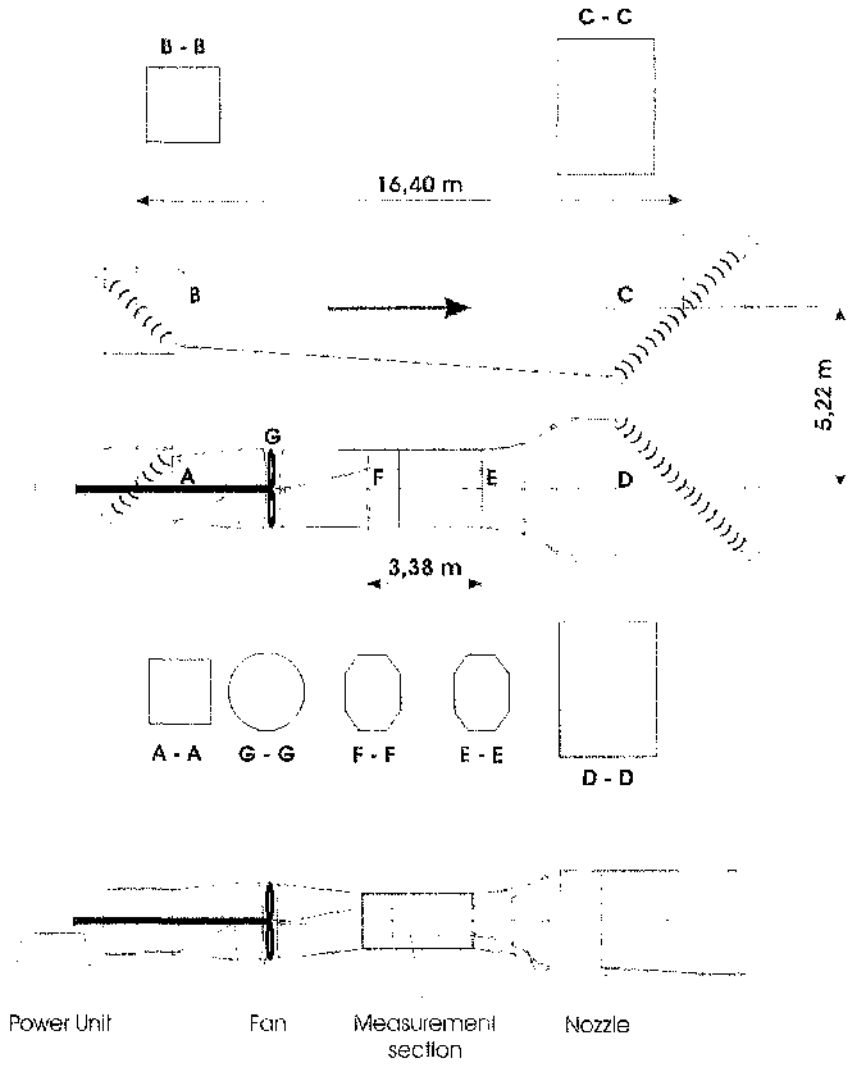


Figure 7. Handley Page wind tunnel circuit

Dimensions of the wind tunnel cross-sections [mm]:

| | | | |
|---|---|---|---|
| A-A | 1900 x 1900 | E-E | 1600 x 2150 |
| B-B | 2200 x 2200 | F-F | 1600 x 2150 |
| C-C | 3000 x 4000 | G-G | diameter 2300 |
| D-D | 3000 x 4000 | | |

## 2.2 Wind Tunnel Test Configuration

### 2.2.1 Measurement Procedure

The measurement chain consists of x-wire sensor, a TSI IFA 300 constant temperature anemometry system, a personal computer, a SMOCI transmitter and a traversing mechanism as shown in Figure 8.

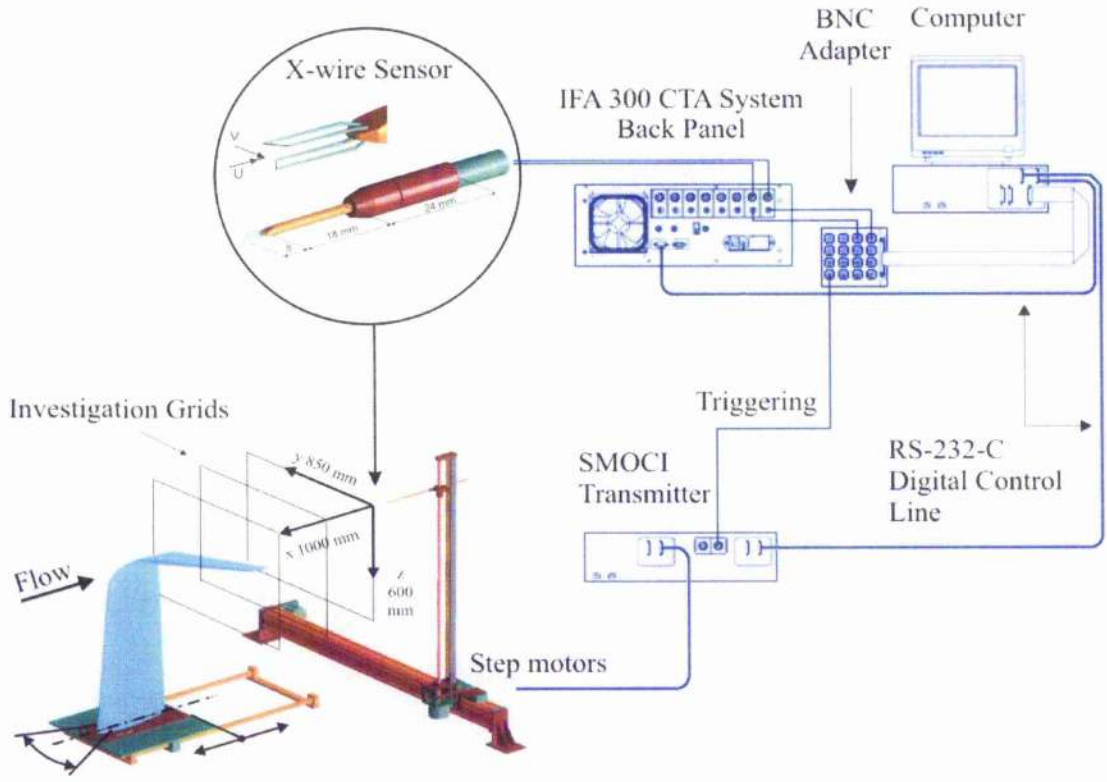


Figure 8. Wind tunnel test configuration

The X-wire sensor is connected to two channels of the IFA 300 by coaxial cables. The IFA 300 hardware converts the acquired signals from the sensors and transmits them to the controlling computer via a BNC adapter block and data acquisition card. The IFA 300 software installed on the computer processes the recorded data. Once the data have been recorded for an entire Y traverse, a master program, written in

LABView, sends a new instruction to the SMOCI unit. The SMOCI transmitter converts the instruction into the signal needed by the stepper motors to move the traverse to its next Z position. When the traverse mechanism reaches this new position, another signal is sent to it and it begins its Y traverse. The x-wire sensor continually samples data during this traverse and sends the signal to the computer. This process continues until measurements have been made over the entire measurement grid. The models were mounted vertically on a base plate that was secured to a rail track mechanism (Figure 9). This mechanism allowed the model to be moved backwards and forwards in the wind tunnel working section to change the distance between the model and the hot-wire measurement plane. In addition, the base plate was designed to allow the incidence of the model to be changed.

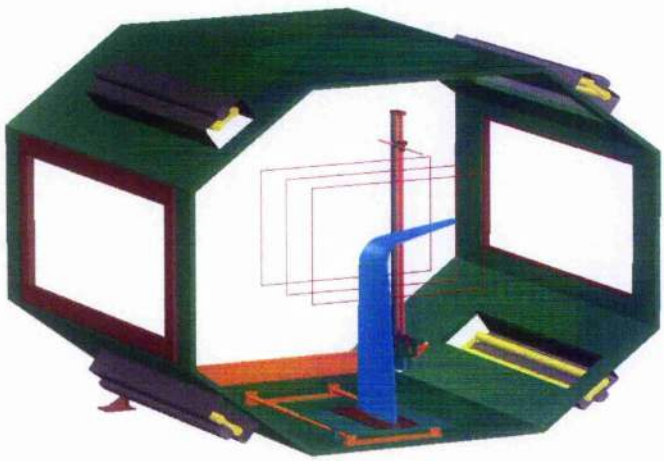

Figure 9. Wind tunnel test section and winglet model position

### 2.2.2 Traverse Mechanism

The computer controlled traverse mechanism for probe positioning and data acquisition was specifically designed and manufactured for the present project.

The traverse is a motorized two-component mechanism that can move the probe to any point within a 850 mm x 930 mm grid. In the present series of tests the traverse mechanism was mounted behind the test models such that measurements could be made in planes perpendicular to the onset flow. The location of the measurement plane with respect to the test model could be varied using the model mounting tracks stated previously. The horizontal motion is provided by a large, off-the-shelf linear slide driven by a stepper motor (Figure 10). Vertical movement is provided by a purpose built traverse mechanism based on a precision ball screw, which is positioned in front of a linear slide mounted on an aluminium box-section support. The carriage of the ball screw is connected to the carriage of the linear slide and so, when the ball screw is driven by a stepper motor, the carriage moves up and down. The incremental resolution of the linear motion is 0.03 mm.

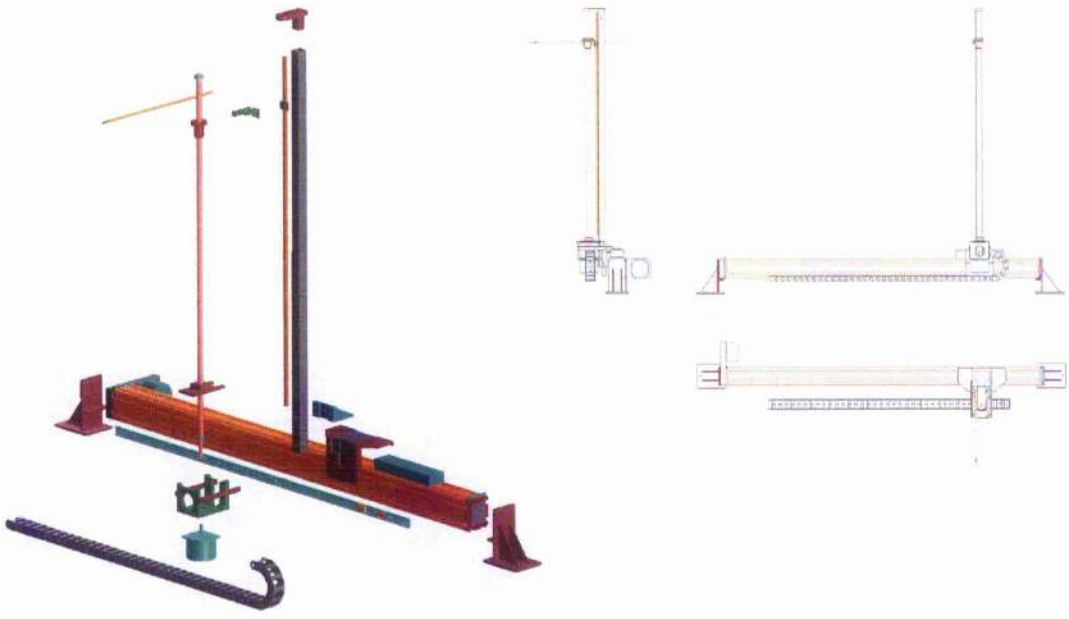

Figure 10. Traverse mechanism

The traversing mechanism was located near the exit of the test section and mounted to the laboratory ground through a frame. The frame carrying the traversing mechanism had no connection to the wind tunnel walls.

The way in which the traverse is assembled is shown in Figure 10 above and Figure 11 shows the assembled traverser in the wind tunnel together with a winglet model.

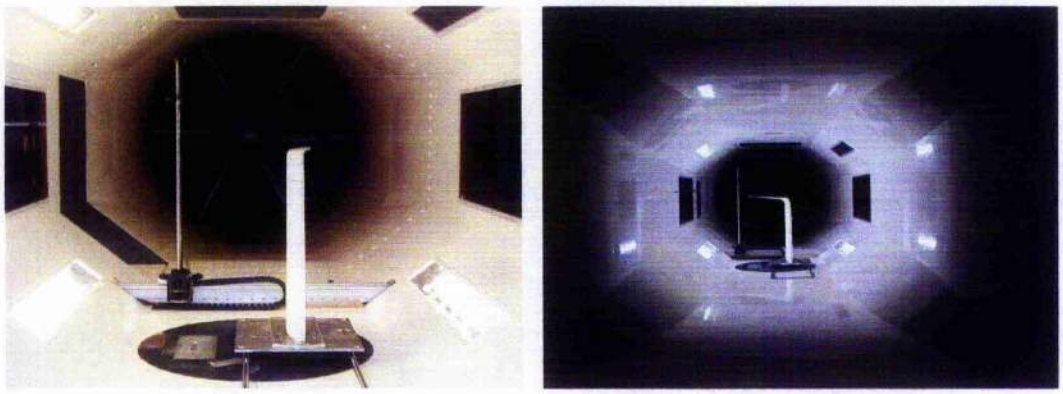

Figure 11. Winglet models (1:1) placed in Handley Page wind tunnel

### 2.2.3 Hot Wire Anemometry

The hot-wire anemometer uses a small, electrically heated element exposed to a fluid medium (e.g. air flow) to analyze the flow field. A wire was used as the heated element during all testing. Since the wire is sensitive to heat transfer between the wire and its environment, temperature changes of the wire can occur. The velocity of the air is measured by its cooling effect on the heated sensor. The hot-wire sensor is able to read instantaneous values of the velocity up to high frequencies. A two-wire sensor is capable of measuring two velocity values and their directions as well as the turbulent fluctuations in the flow field. The Constant Temperature Anemometer (CTA) method is based on the fact that the sensor's resistance will be proportional to the temperature of the wire (3). A feed-back loop in the IFA 300 System (Figure 12)

maintains the wire at a constant temperature (voltage). When the sensor is placed in a flow, the air flowing over the wire will try to cool it. In order to keep the temperature (wire's resistance) constant, the voltage will have to be increased. If the flow is faster, the voltage will be higher. Therefore, the output of the sensor wire represents the instantaneous velocity in the flow.

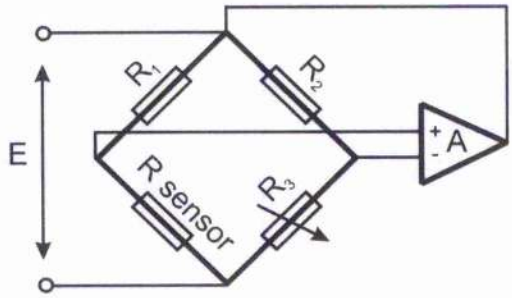


$$Q = IE = I^2R = E^2/R \qquad (3)$$

Figure 12. CTA bridge

Measurements of the magnitude and associated direction of the time-dependent velocities behind the winglet models were obtained using a DANTEC 55P61 cross-wire probe connected to a TSI IFA-300 three-channel constant temperature anemometer system (Figure 13). The sensor wires on the probe are 0.005 mm diameter platinum plated tungsten wires with a length/diameter ratio of 250, which form a measuring volume of approximately 0.8 mm in diameter and 0.5 mm in height. The wires are positioned perpendicularly to each other corresponding to 45 degrees from the free stream direction which gives the best angular resolution.

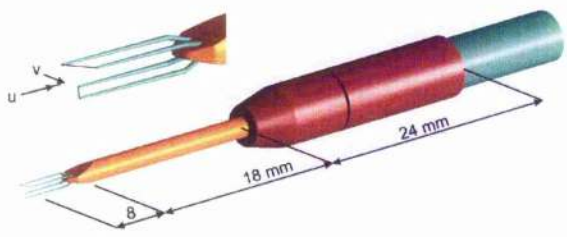


Figure 13. X-wire sensor Dantec 55P51

An additional temperature probe was used to correct the anemometer output voltages for any variation in ambient flow temperature. For probe calibration, an open jet vertical wind tunnel with a maximum operating velocity of 43 m/s was used. A support allowed the sensors of the X-wire probe to be rotated by 30 degs in the plane of the sensors. Variation of the flow velocity and yaw angle then enabled the coefficients of the effective velocity method to be determined (Appendix E).

Figure 14 shows how the hot-wire anemometry system was integrated into the overall measurement system.

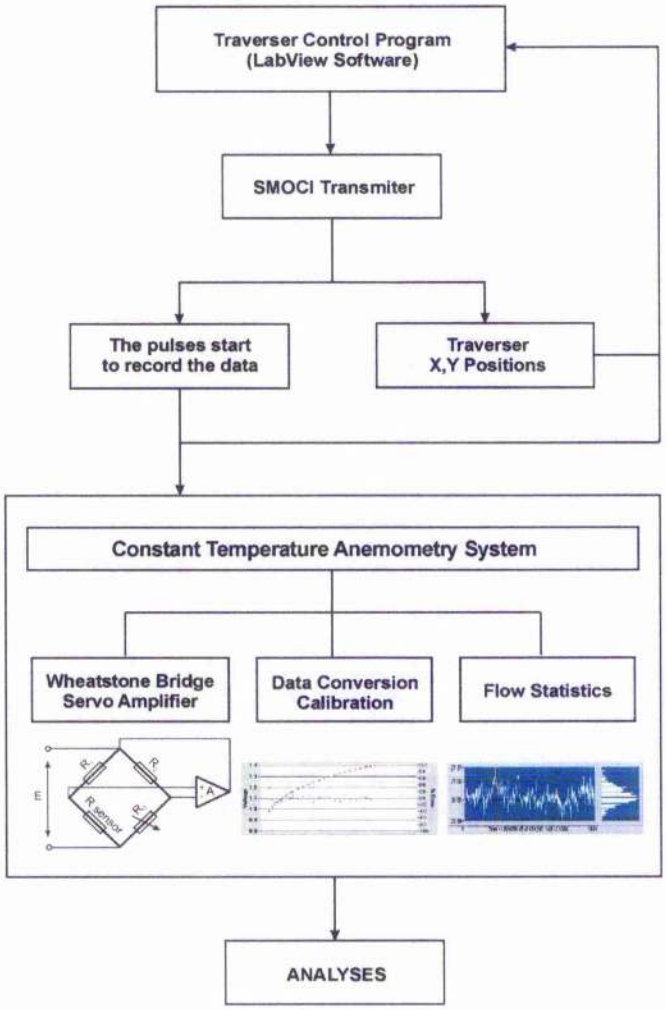


Figure 14. Flow chart of data acquisition

## 2.2.4 Investigation Grid

**Y-travel:**

One step of the stepper motor provided 0.03125 mm of linear motion and the time required for each step was 0.2980 miliseconds. The size of the investigation grid in the y-direction was 850 mm (Figure 15) or 27200 steps of the stepper motor. The time required to traverse this distance was, therefore, 8.1055 sec.

At a sampling rate of 2000 Hz, the sampling time of 8,1055 seconds gives a total of 16211 investigation points per line. To allow for turbulence in the flow, the data are averaged in blocks of 48 measurement points corresponding to approximately 2.5 mm of motion. Thus, 339 averaged data values are collected during each Y traverse.

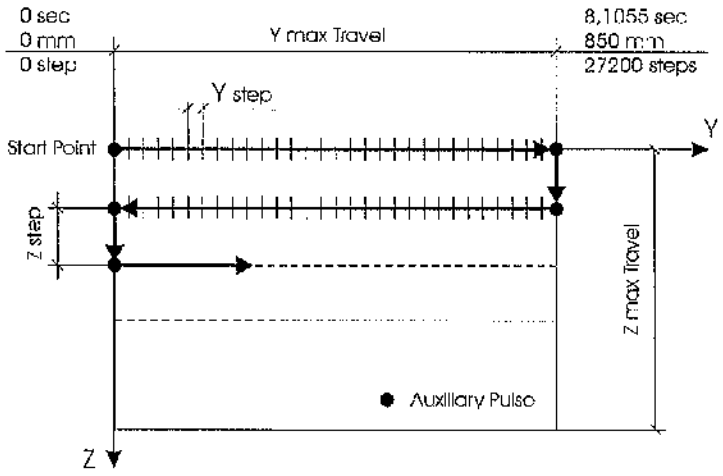


Figure 15. Investigation grid

**Z-travel**

The length of the investigation grid in the Z-direction was set at 600 mm. This length was divided into steps of 5 mm giving a total of 121 measurement points in the Y direction. The total time taken to traverse the entire 850 mm x 600 mm grid was just over 20 minutes and a total of 41019 measurements were obtained for each grid. A schematic of this process is presented in Figure 15.

### 2.2.5 Wind Tunnel Models of Winglets

The wind tunnel models used in the experiments were real wing tips taken from the single seat, HpH 304CZ/C sailplane's wings (Figure 17). The models were mounted vertically on a base plate that was secured to a rail track mechanism. This mechanism allowed the model to be moved backwards and forwards in the wind tunnel working section to change the distance between the model and the hot-wire measurement plane. In addition, the base plate was designed to allow the incidence of the model to be changed.

During the experimental program four types of wing tips were investigated; a wing without a winglet and then three 304CZ sailplane wing tips of different design. The key parameters that defined the winglet designs are shown in Figure 16 and are the winglet airfoil, sweepback, cant angle, twist distribution and ratio of winglet root chord to winglet tip chord (taper). Details of the sailplane itself and photograph of the test models are provided in Figures 17 an 18 respectively.

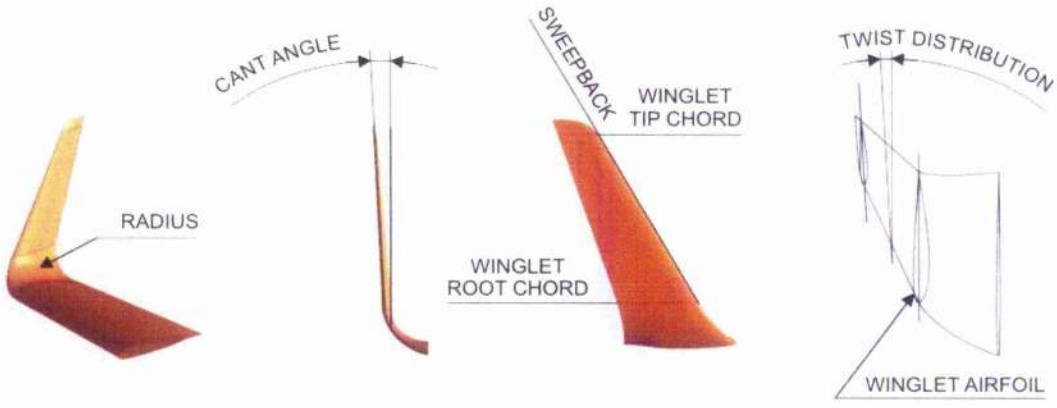


Figure 16. Key design parameters of winglets

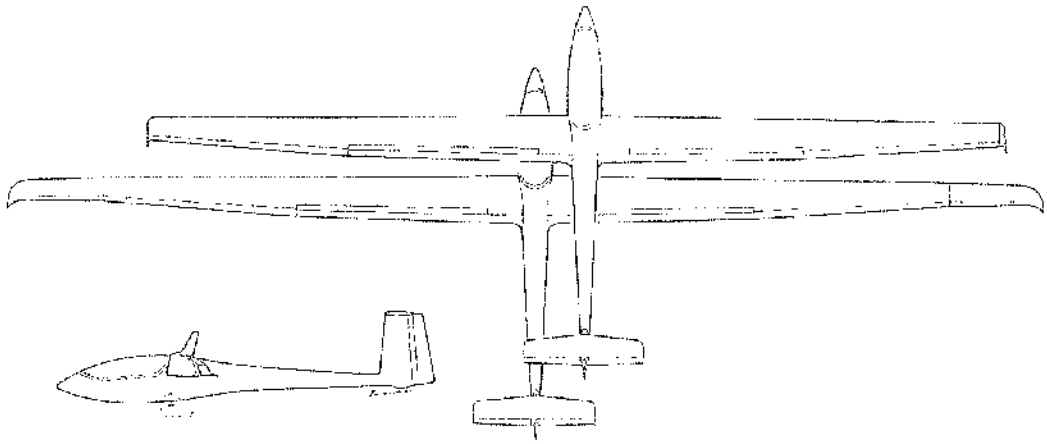

Figure 17. Sailplane HpH 304 CZ, 304C Wasp

| Model / Configuration | 304CZ<br>FAI 15 meter class flapped glider | 304C Wasp<br>FAI standard class glider |
|---|---|---|
| Material | CfC | CfC |
| Number of seat | 1 | 1 |
| Dimensions | | |
| Wing | | |
| Span | 15m / 49.21 ft | 15m / 49.21 ft<br>(17.4m - with tip extensions) |
| Area | 9.88 m2 / 106.35 sqft | 9.90 m2 / 106.59 sqft |
| Aspect Ratio | 22.78 | 22.80 |
| Wing Airfoil | | HQ 010-1642 |
| Fuselage | | |
| Length | 6.45m / 21.16 ft | 6.45m / 21.16 ft |
| Height | 1.36m / 4.46 ft | 1.36m / 4.46 ft |
| Weights | | |
| Empty | 235kg / 518.0 lb | 235kg / 518.0 lb |
| Max. AUW | 450kg / 992.07 lb | 450kg / 992.07 lb |
| Max. Wing loading | 45.55 kg/m2 / 9.33 lb/ft | 45.45 kg/m2 / 9.32 lb/ft |
| Min. Wing loading | 30.80 kg/m2 / 6.31 lb/sqft | 30.80 kg/m2 / 6.31 lb/sqft |
| Waterballast | 115L / 30.37 gal | 115L / 30.37 gal |
| Wt. Non lifting Parts | 300kg / 661.4 lb | 300kg / 661.4 lb |
| Limitations | | |
| VNE | 250km/h - 155.35 mph | 250km/h - 155.35 mph |
| Stall speed (at max AUW) | 73km/h - 45.36 mph | 73km/h - 45.36 mph |
| min. sink | 0.56 m/s - 1.83 ft/sec | 0.57 m/s - 1.86 ft/sec |
| at speed - normal wt | 60 km.h - 37.30 mph | 77 km.h - 47.85 mph |
| Best L/D (at max AUW) | 44 | 42.7 |
| at speed | 73 km/h - 45.36 mph | 116 km/h - 72.08 mph |

Tab. 1. Technical data of HpH 304CZ, 304C Wasp sailplane

Options:

Standard wing tip, detachable winglets and wing tips for 17.43 meter (Figure 18)

| | |
|---|---|
| Wind tunnel model A: | HpH 304 sailplane's standard wing tip |
| Wind tunnel model B: | HpH 304 sailplane' s detachable winglet |
| Wind tunnel model C: | HpH 304 sailplane's winglet |
| Wind tunnel model D: | HpH 304 sailplane's wing tip for 17.43 meter span |

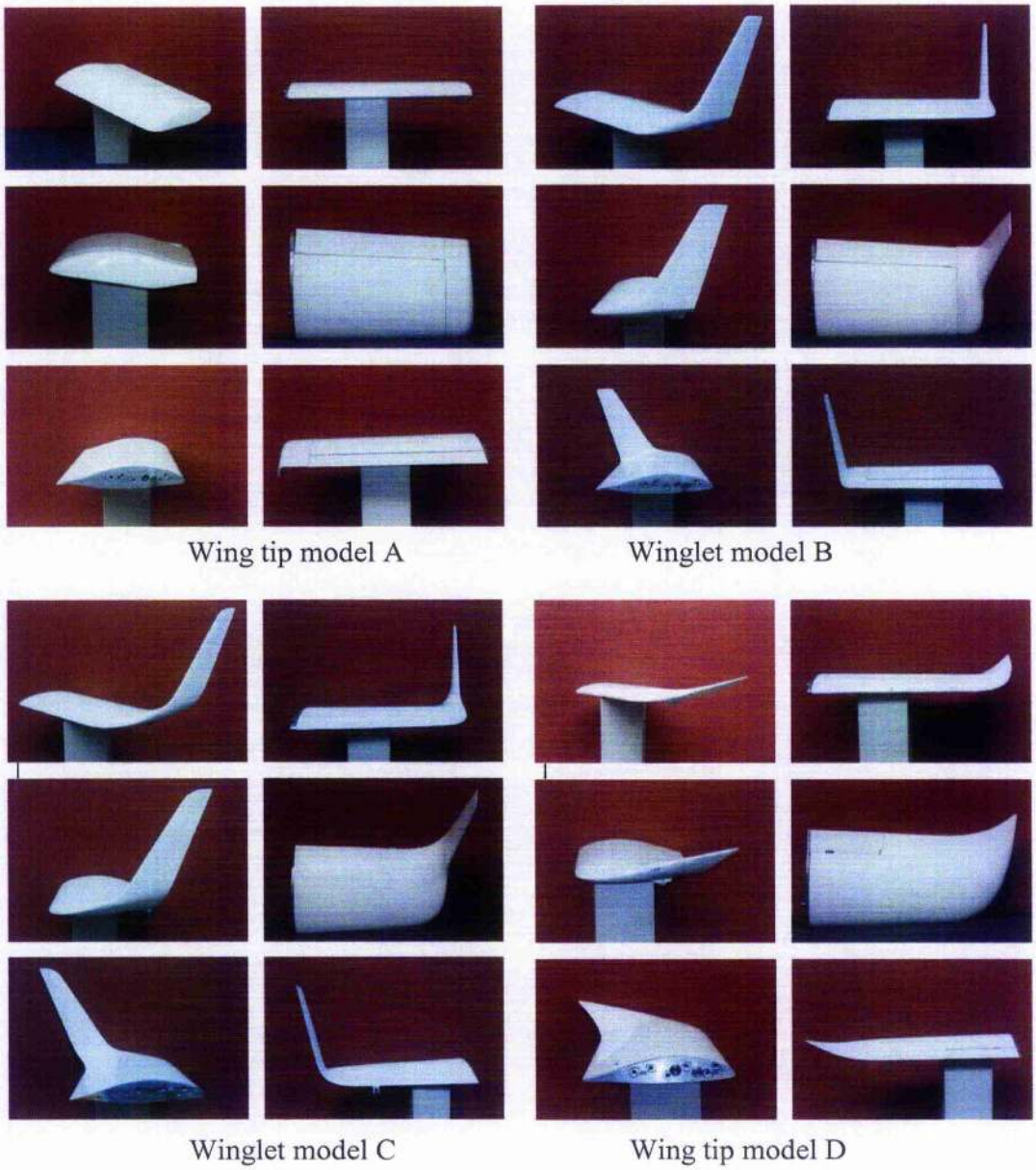

Wing tip model A Winglet model B

Winglet model C Wing tip model D

Figure 18. Wind tunnel wing tip models

# Chapter 3

## 3. Experimental Results

This chapter presents the measurements of the 3-dimensional vortex structures created by the various wing tip geometries, with data presented using Tecplot software.

Figures 19-35 present measured data for four wing tip configurations in three planes (x/b= 0.2, 1 and 2) with the wings at angles of attack $\alpha$ = 0, 3, 6 degrees (alternatively 9 degrees) at a free stream velocity $U_\infty$= 33 m/s.

The vortex structures have been examined by measuring the U, V and W velocity components in 3 planes perpendicular to the wind tunnel axis.

The diagrams in figures 22, 26, 31, 35 give the location of the downstream wake (the regions containing decelerated particles having passed through the boundary layer). The domains have been selected from the matrices of measured points by suppressing velocities of the free stream value and higher.

## 3.1 Results I: Wing Tip Model A

### 3.1.1 Observations

*Configuration:*

Wing tip A is basically a standard wing tip with a small vertical extension that projects downwards from the lower surface of the wing. This small extension protects the wing tip against damage during the sailplane's take-off.

Distributions of flow field parameters contained in figures 19 -22 show:

*Vortex core location:*

When the angle of attack is increased the vortex is deflected slightly downward. The vortex core does not change its position in the z direction, leaving the vortex parallel to the free stream flow.

*Vorticity volume:*

The tip vortex size increases with increasing angle of attack and with downstream distance.

Vorticity in the wake of the main wing gradually increases when the angle of attack increases. On the other hand the vorticity level in the wake gradually decays when moving downstream.

The vorticity decrease in the wake behind the wing trailing edge corresponds to the tip vortex increment. This is consistent with the roll-up process when the vorticity becomes more concentrated in a single tip vortex.

The location of the vorticity area generally changes with distance behind the wing.

*Downwash effect:*

The pictures in figure 22 show the downstream wake position. The trailing wake behind the wing moves downward as a result of the induced velocity distribution. Increasing the angle of attack causes an increase in induced velocity and thus stronger downwash.

### 3.1.2 Vector Plots of Velocity Distribution and Contour Plots of Vorticity Distribution

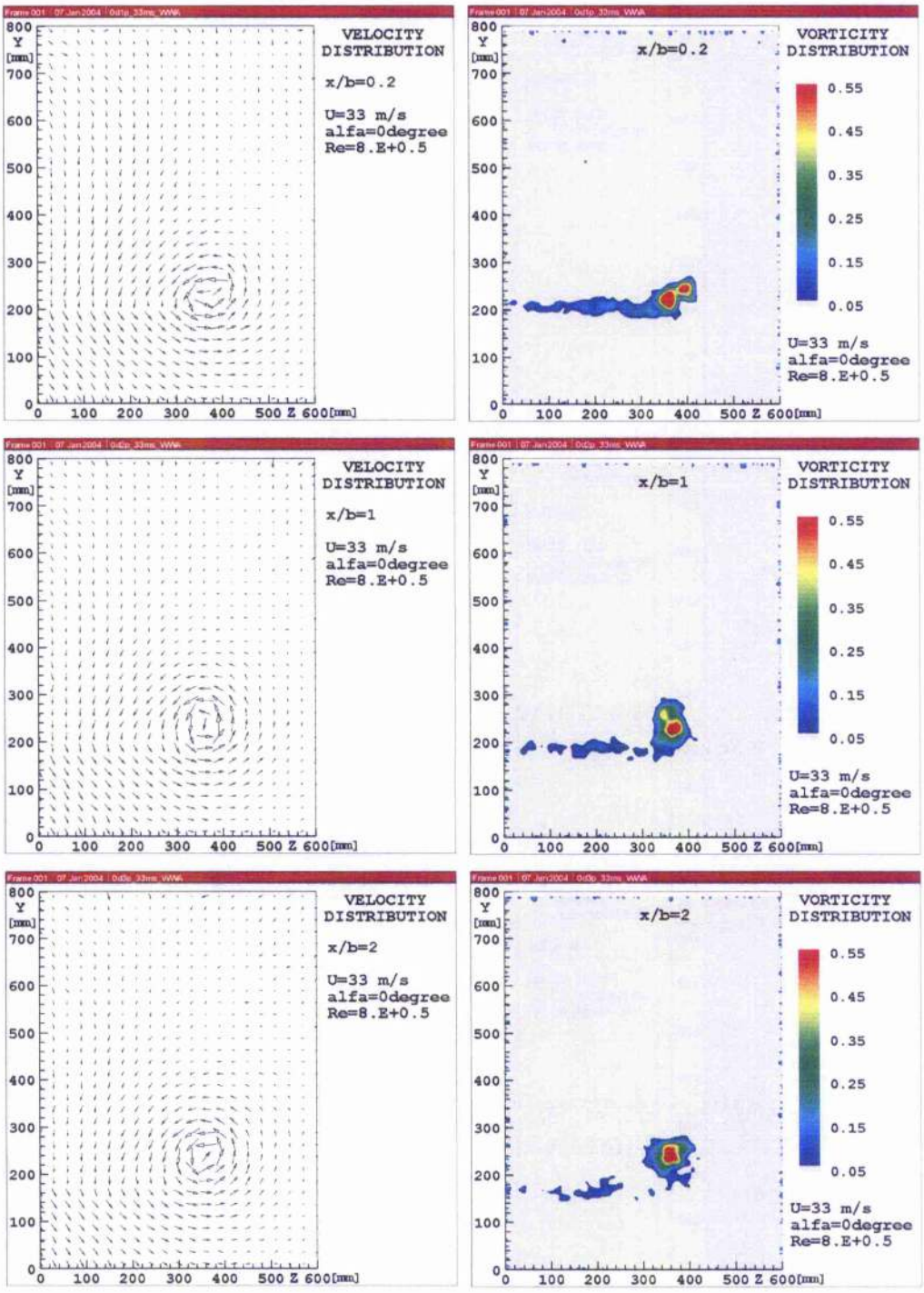


Figure 19. Velocity and vorticity distribution behind wing tip **model A**, angle of attack **0 degrees**.

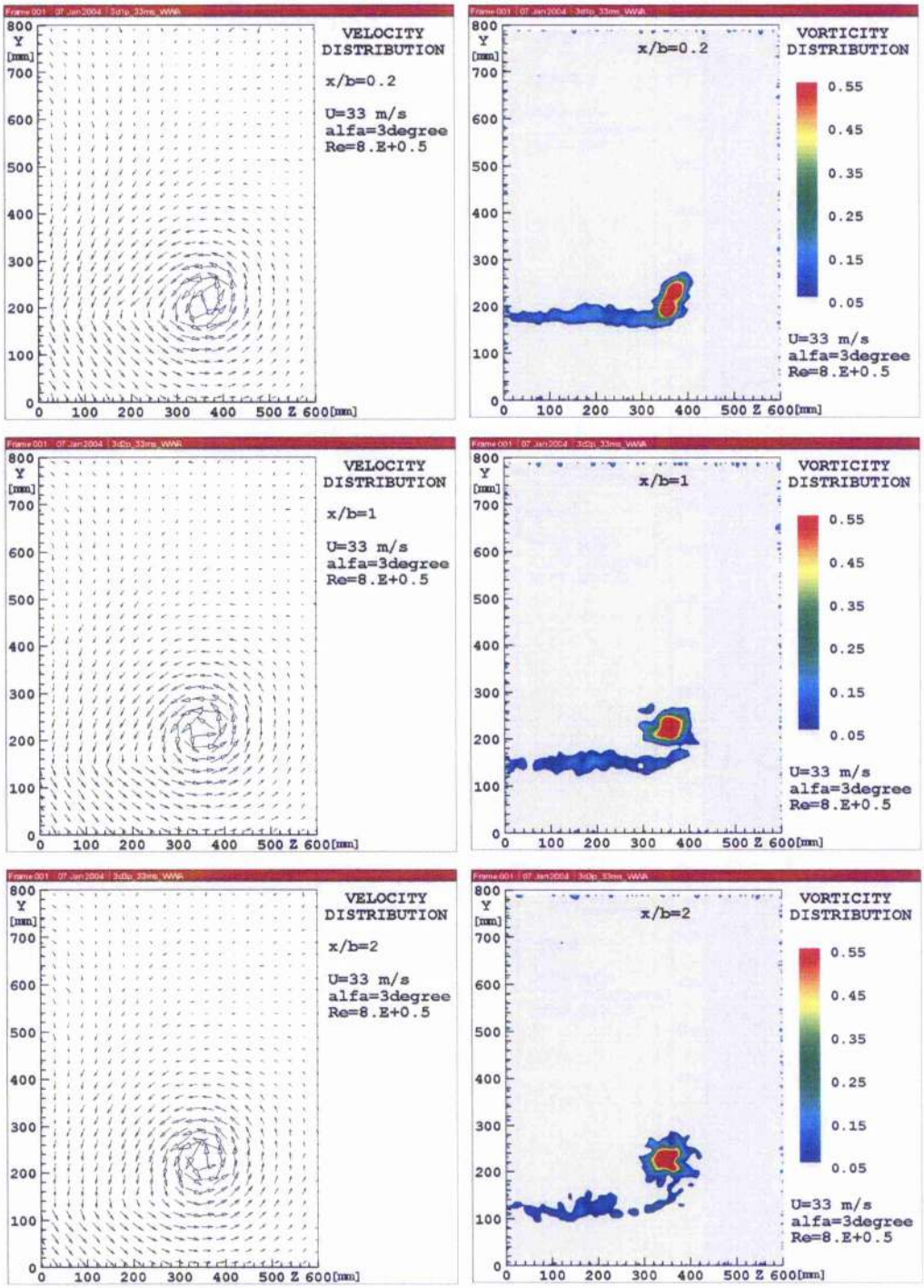


Figure 20. Velocity and vorticity distribution behind wing tip **model A**, angle of attack **3 degrees**.

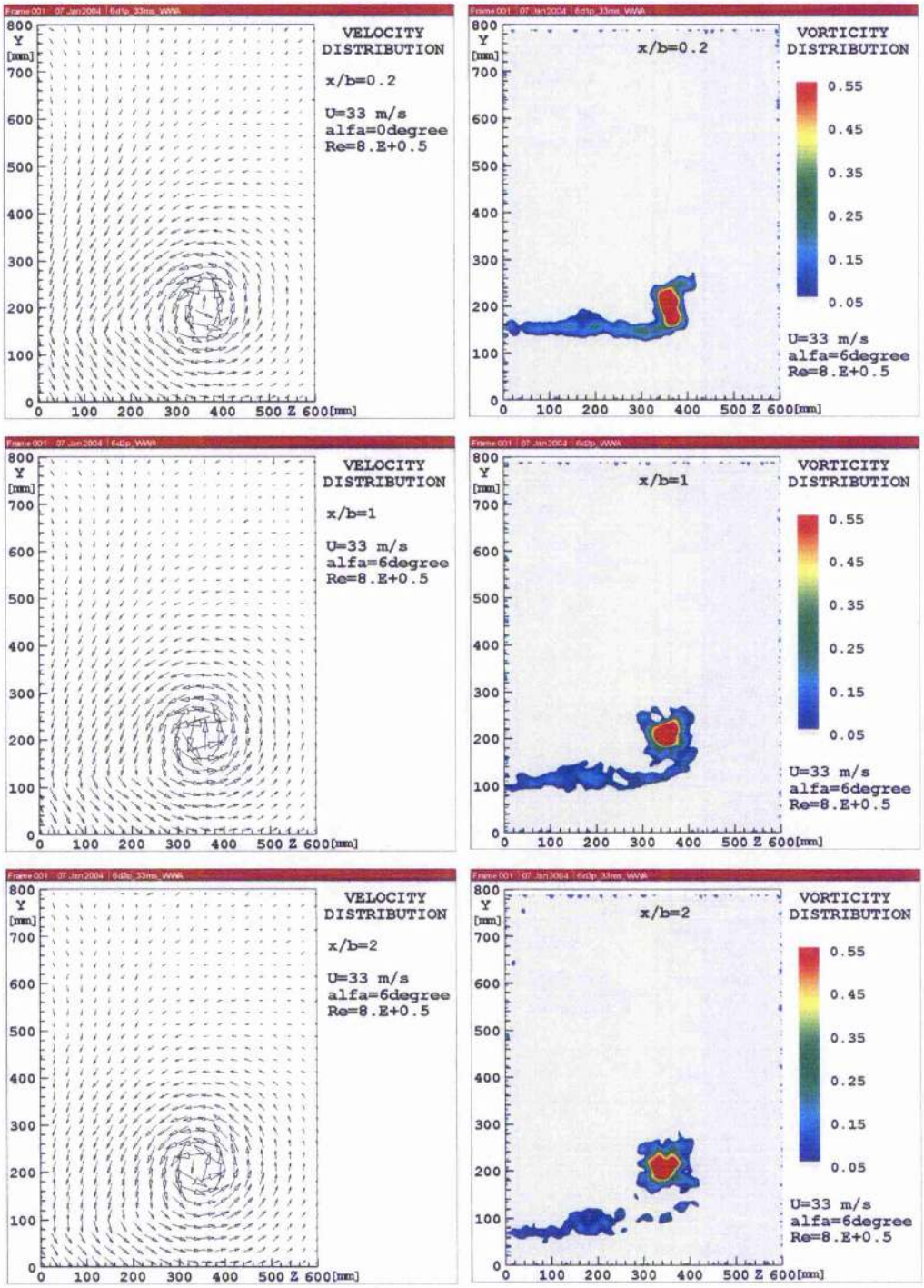


Figure 21. Velocity and vorticity distribution behind wing tip **model A**, angle of attack **6 degrees**.

### 3.1.3 Downstream Wake Position

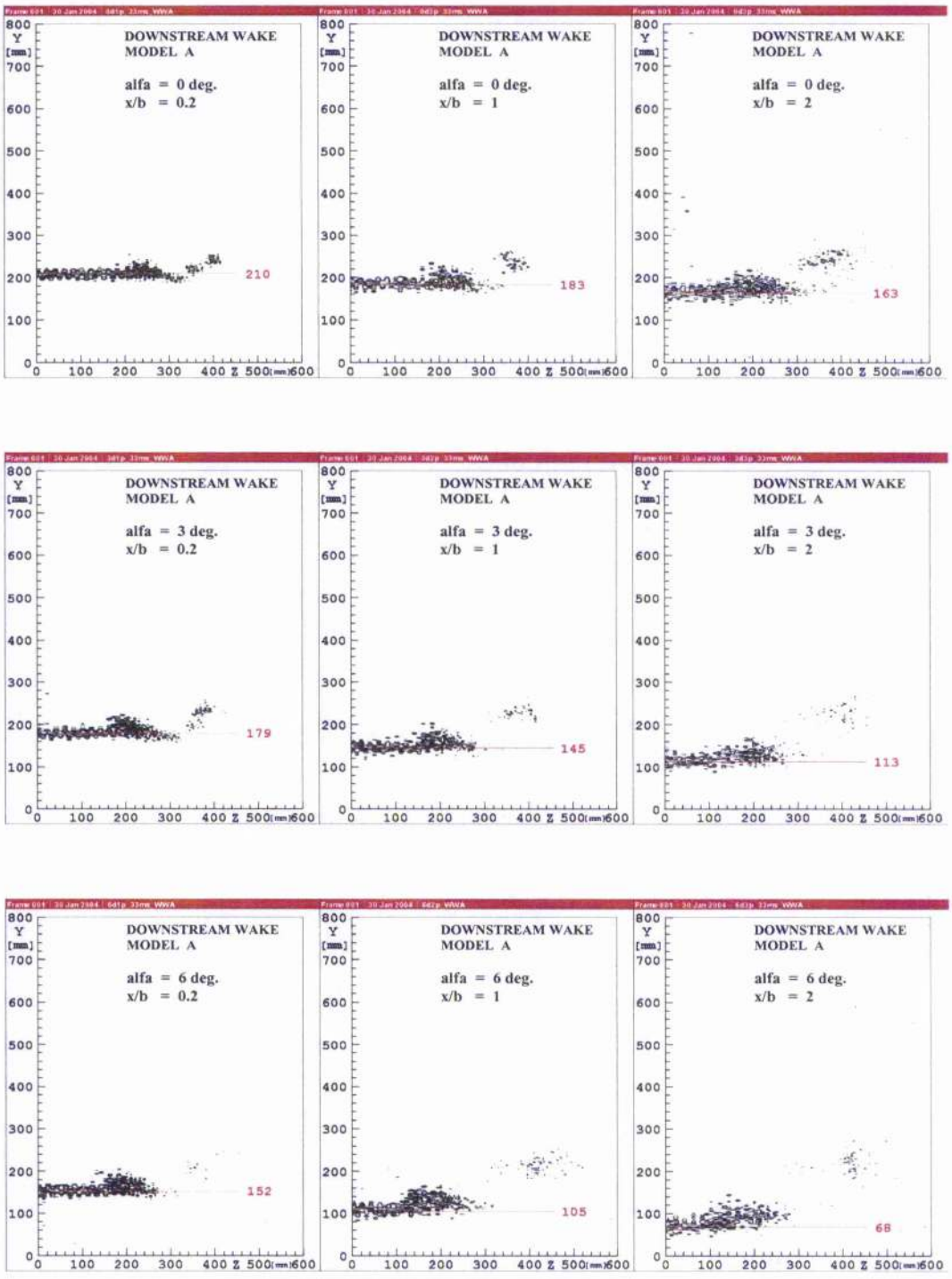


Figure 22. Downstream wake behind wing tip model A

## 3.2 Results II: Winglet Model B

### 3.2.1 Observations

*Configuration:*

The winglet configuration includes 30 degrees of sweep-back, a cant angle of 5 degrees, twist of 3 degrees and a very small radius between the wing and winglet. Distributions of flow field parameters contained in figures 23 -26 show:

*Vortex core location:*

In this case, there are two clear separated vortex structures: One at the wing/winglet junction and the other at the tip of the winglet.

Results show the roll-up process. The vortex core at the wing/winglet junction moves outboard as opposed to the winglet tip vortex which moves inboard.

*Vorticity volume:*

The vorticity area between the tip vortex and the junction vortex does not appear to change its intensity with changing angle of attack. This effect corresponds to the theory which suggests that higher vorticity level, in this region would require an increase in cant angle. It is also evident that the vorticity area gradually decays with distance downstream and rotates slightly in the direction of rotation of the tip vortex. Compared to model A, the vorticity behind the wing trailing edge is almost non-existent, contrary to the wake behind the winglet where the vorticity is very pronounced.

*Downwash effect:*

The downstream effect is significantly different to model Λ in terms of the movement of the main wing wake. This is indicative of the impact of the winglet on the distribution of induced velocity.

### 3.2.2 Vector Plots of Velocity Distribution and Contour Plots of Vorticity Distribution

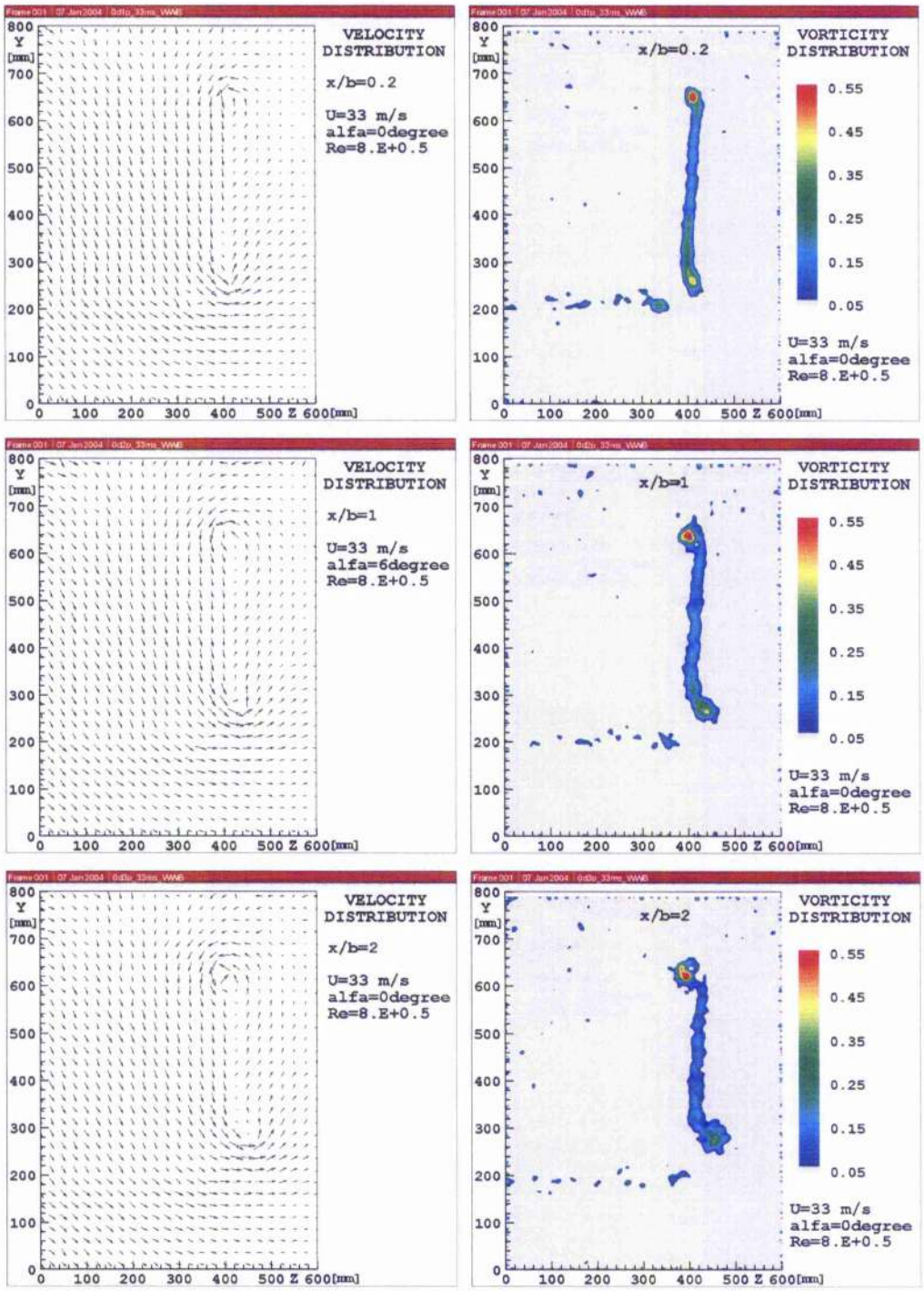


Figure 23. Velocity and vorticity distribution behind winglet **model B**, angle of attack **0 degrees**.

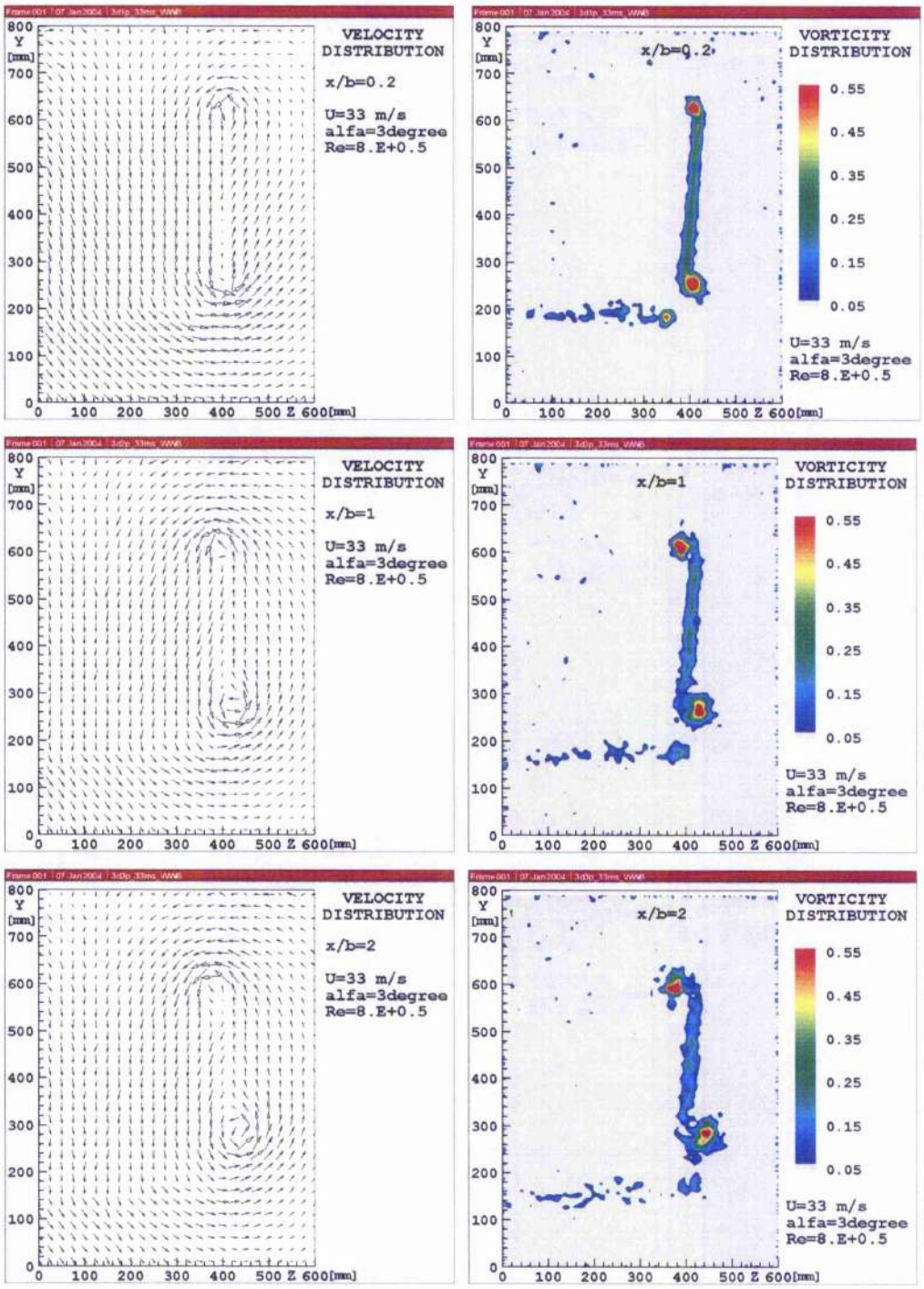


Figure 24. Velocity and vorticity distribution behind winglet **model B**, angle of attack **3 degrees**.

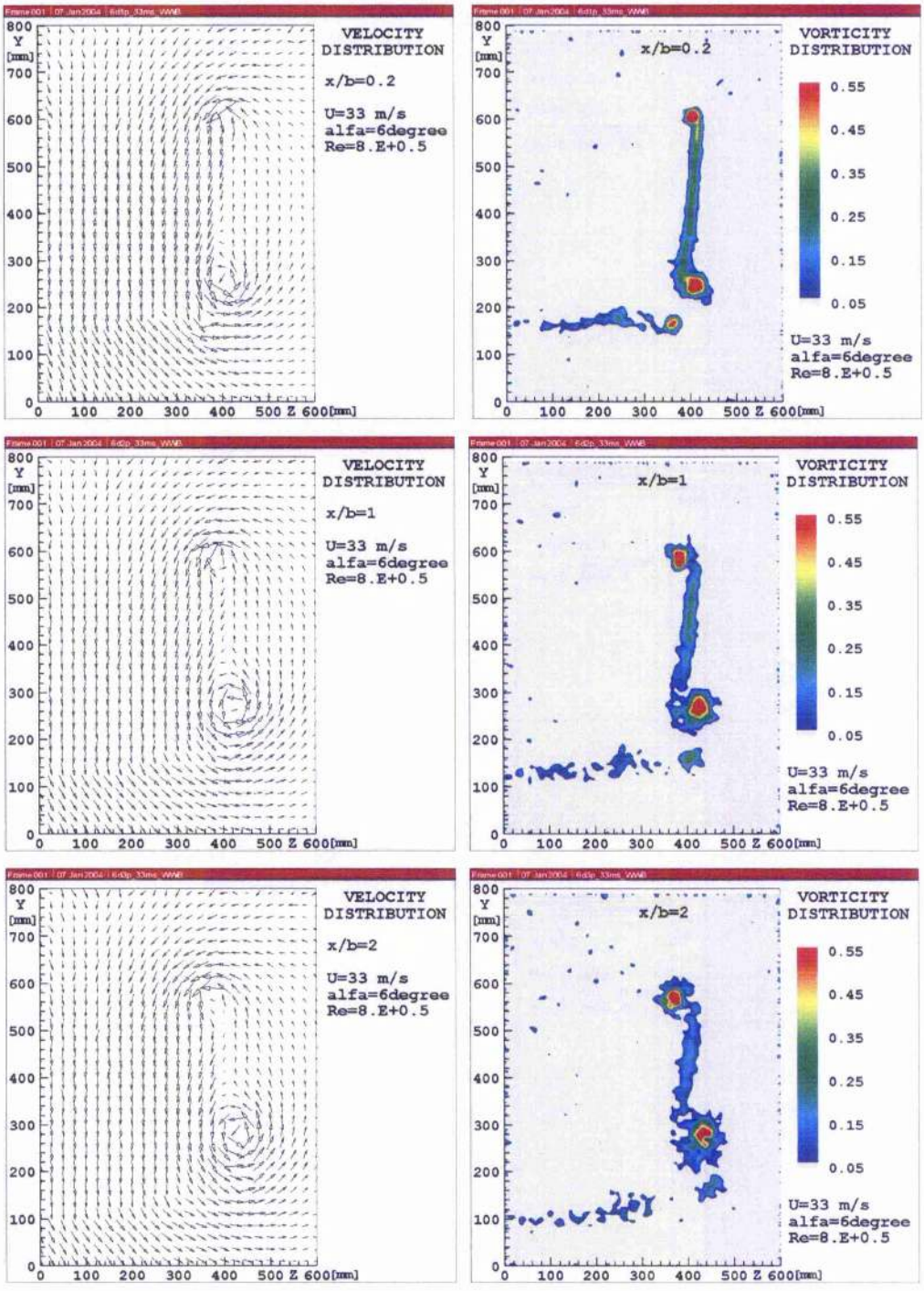


Figure 25. Velocity and vorticity distribution behind winglet **model B**, angle of attack **6 degrees**.

### 3.2.3 Downstream Wake Position

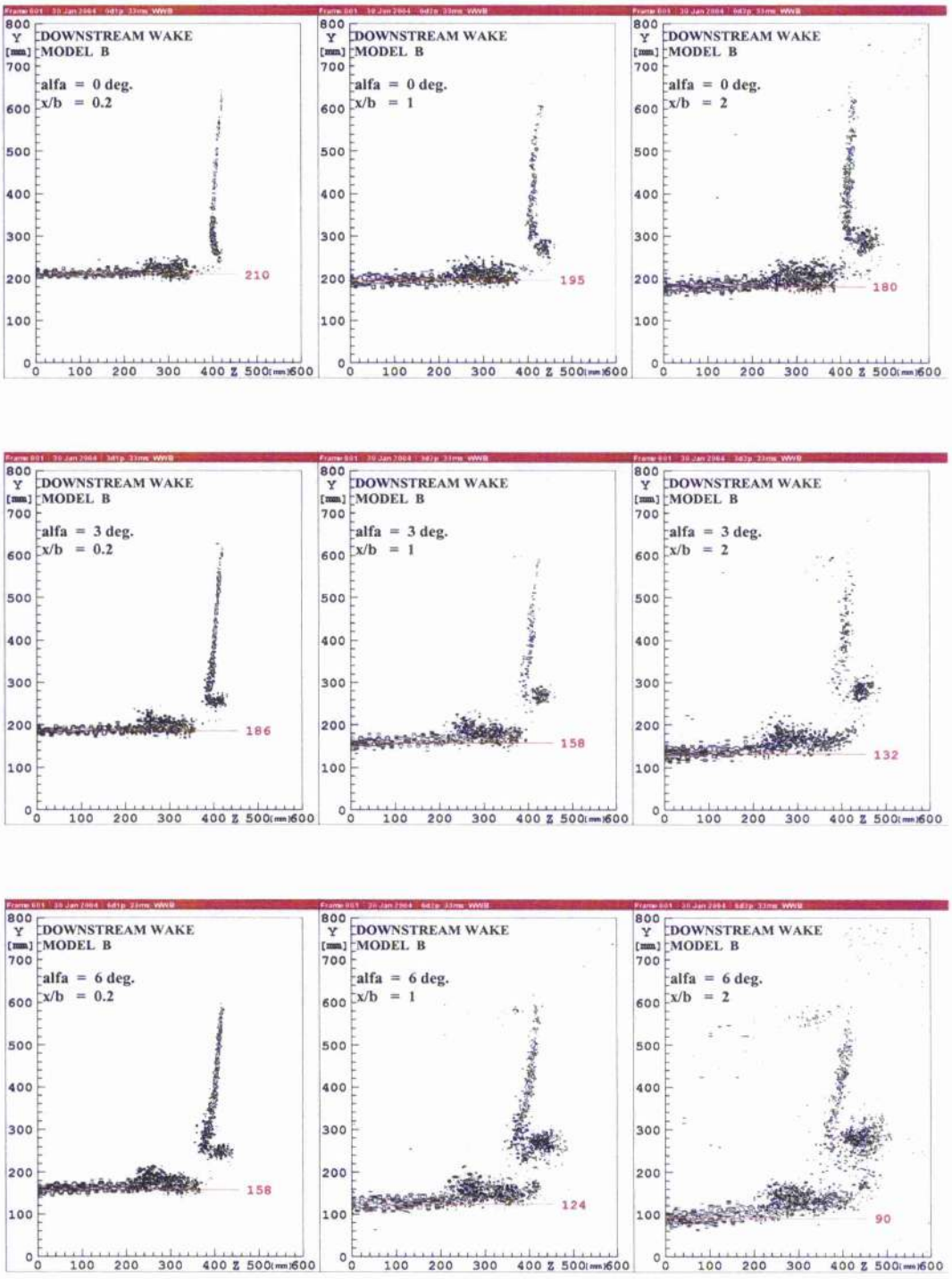


Figure 26. Downstream wake behind winglet model B

## 3.3 Results III: Winglet Model C

### 3.3.1 Observations

*Configuration:*

This winglet configuration has a sweep back angle of 40 degrees, cant angle of 5 degrees, twist of 3 degrees and the wing/winglet junction, compared to model B, is designed to reduce interference effects via a greater radius between the wing and the winglet. The winglet also has a greater taper ratio compared to model B.

The geometry of sweeping the winglet back and higher taper ratio is presented in figures 27 -31.

*Vortex core location:*

The measurements show that both the wing/winglet vortex and the winglet tip vortex move inboard with increasing distance behind the wing. The winglet tip vortex is less distinct, but it should be remembered that the tip of the winglet will be closer to the measurement plane in this case and so the roll-up may not be as complete.

*Vorticity volume:*

In the figures presented, the vorticity associated with the wing/winglet junction does not appear as a single well defined vortex but rather as a more spread-out region of vorticity.

Compared to model B the vorticity levels in each of the measurement planes at low angles of attack are relatively low. In fact, at higher angles of attack, the measured levels are similar to those of model B at lower angles of attack.

The region of vorticity which is clearly visible below the wing tip is the wake behind a small pod which covers a small wheel. This wheel prevents the wing tip from ground impact during take-off and landing.

The outboard shift of the structure as the angle of attack increases is caused by the natural pressure gradient from the pressure side to the suction side of the wing.

The same effect is observed in the flow field past model B

*Downwash effect:*

The vertical position of main wing wake is lower than for model A. This suggests stronger local downwash in the vicinity of the winglet.

### 3.3.2 Vector Plots of Velocity Distribution and Contour Plots of Vorticity Distribution

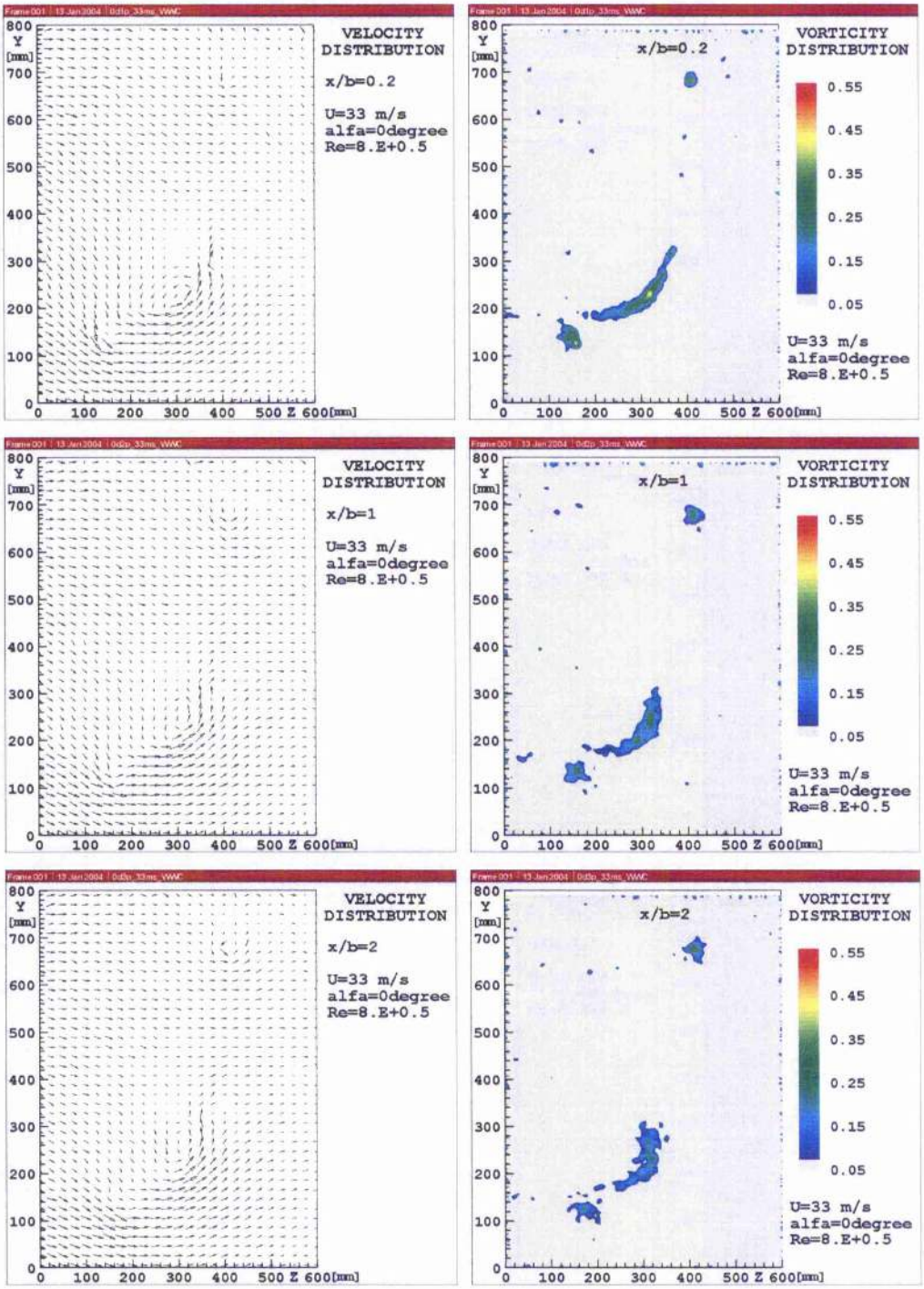


Figure 27. Velocity and vorticity distribution behind winglet **model C**, angle of attack **0 degrees**.

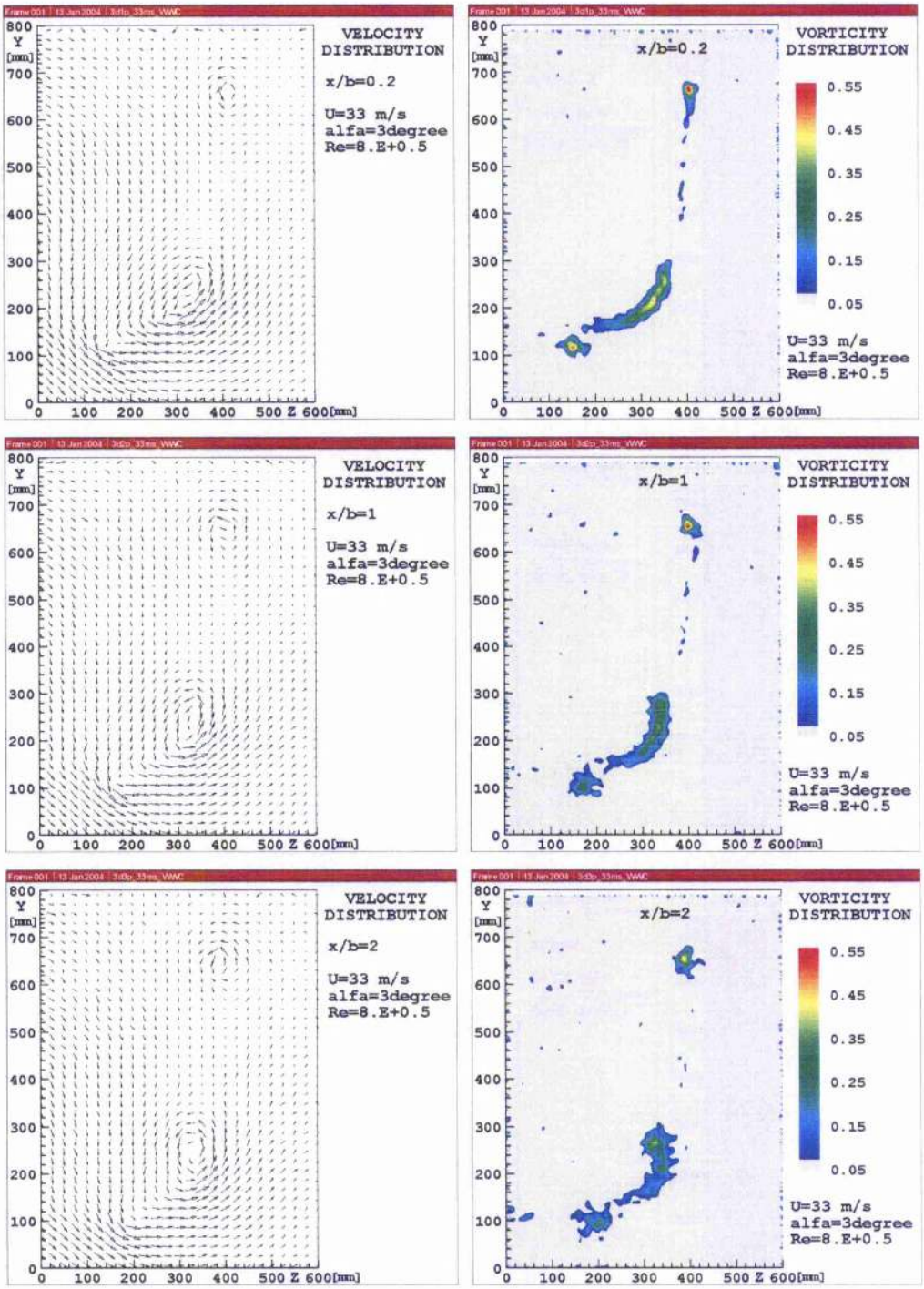


Figure 28. Velocity and vorticity distribution behind winglet **model C**, angle of attack **3 degrees**.

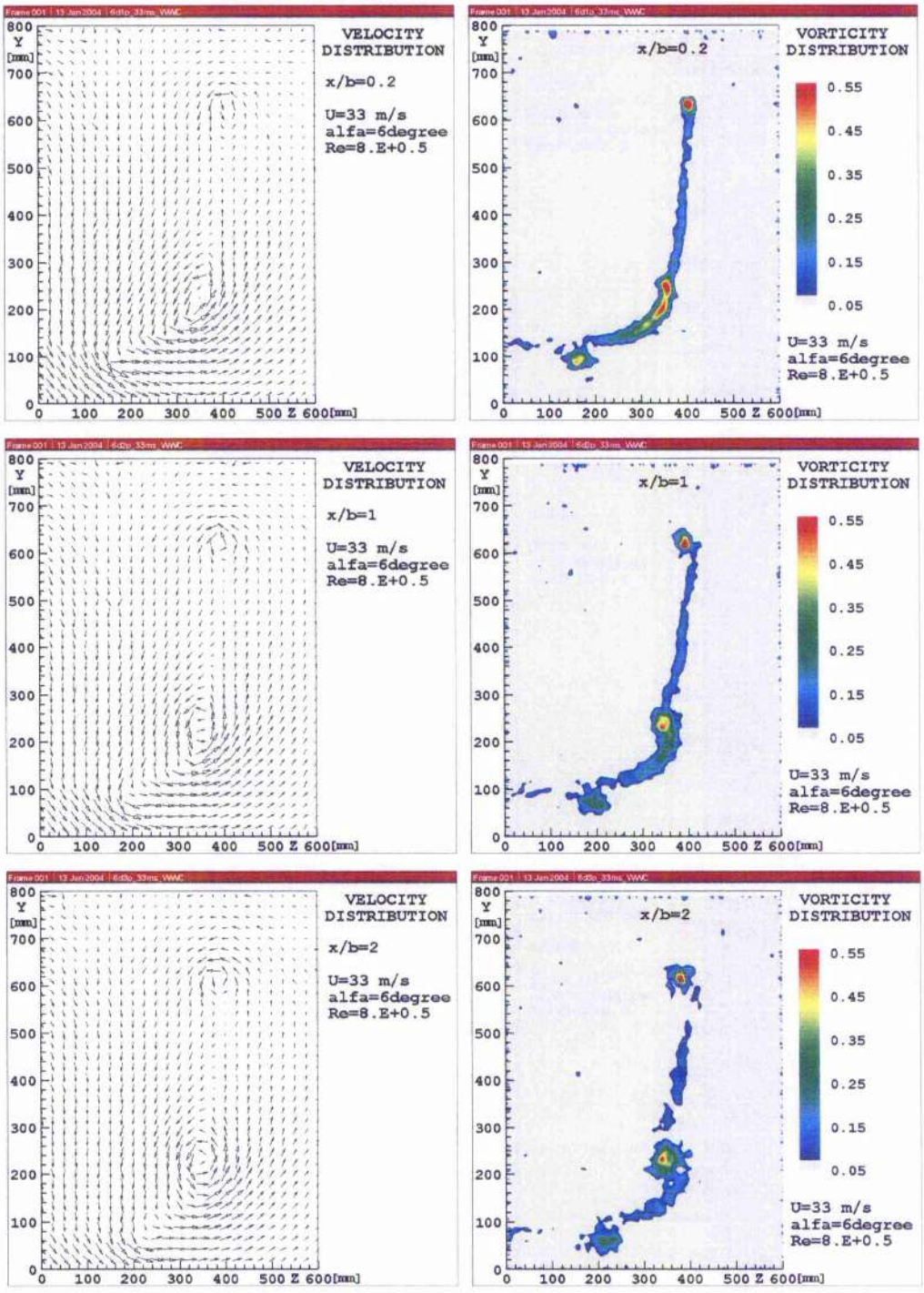


Figure 29. Velocity and vorticity distribution behind winglet **model C**, angle of attack **6 degrees**.

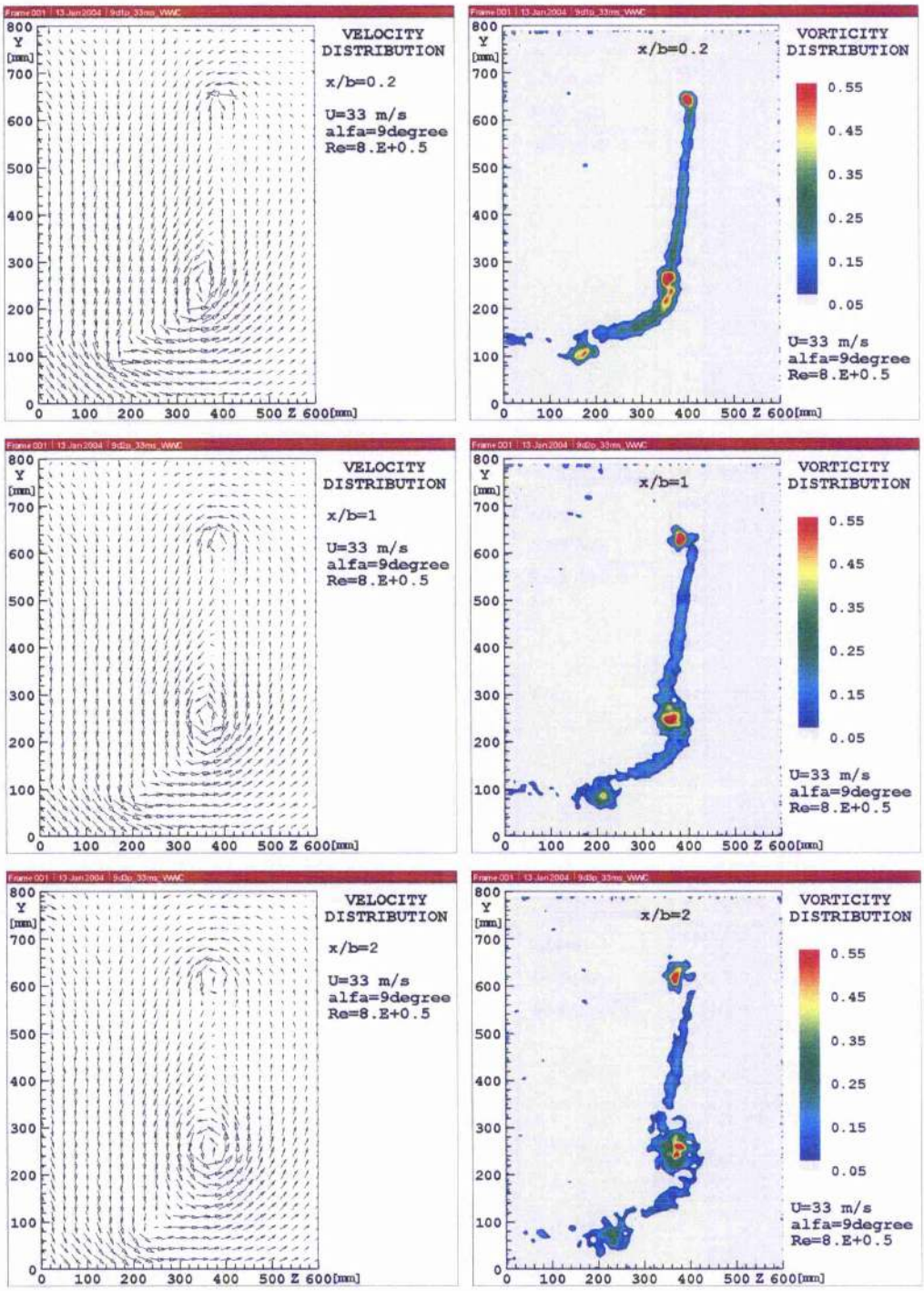


Figure 30. Velocity and vorticity distribution behind winglet **model C**, angle of attack **9 degrees**.

### 3.3.3 Downstream Wake Position

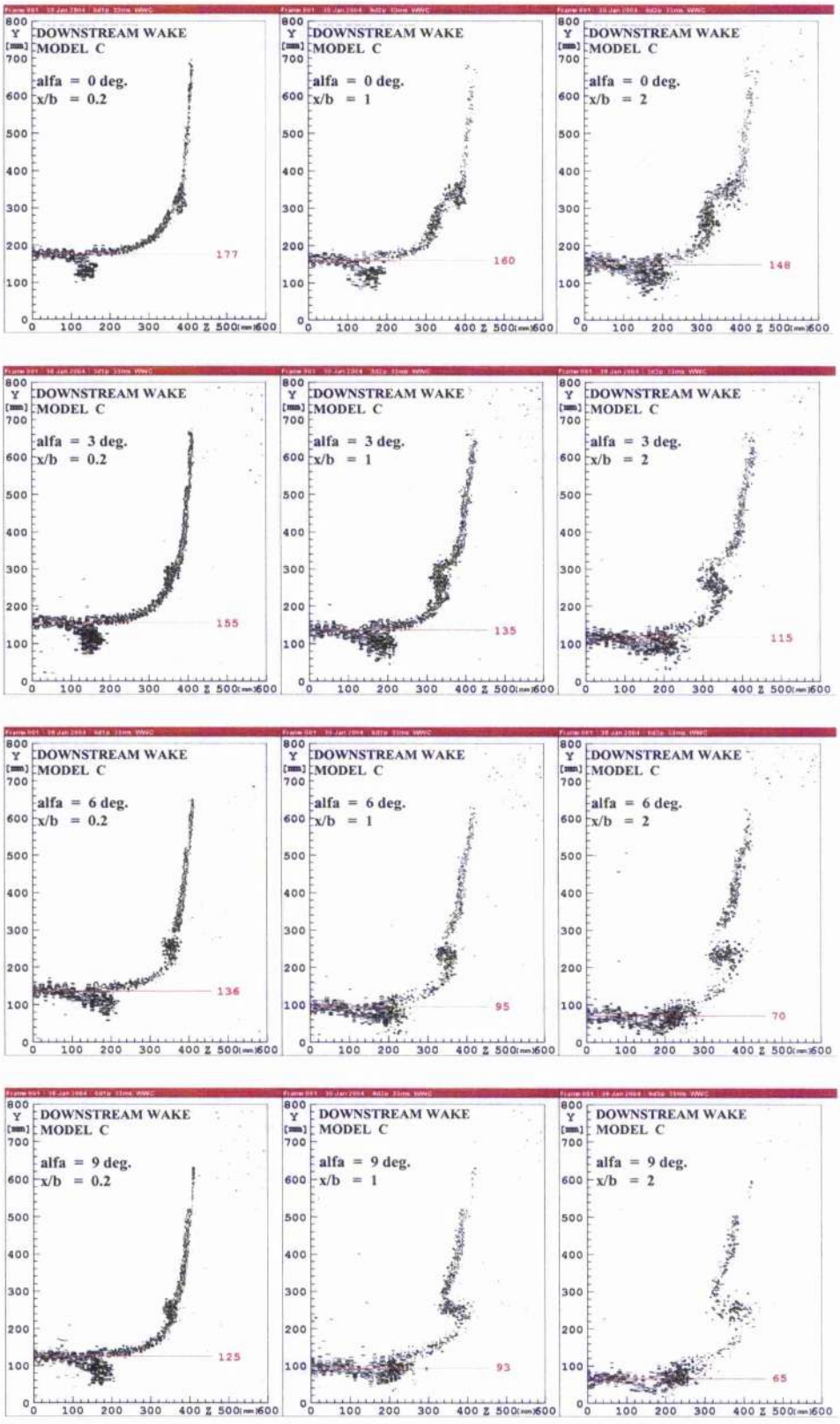


Figure 31. Downstream wake behind winglet model C

## 3.4 Results IV: Wing Tip Model D

### 3.4.1 Observations

*Configuration:*

The model D presents a small upward swept wing tip.

*Vortex core location:*

The vortex core does not develop before an angle of attack of 3 degrees and gradually evolves inboard of the wing tip.

*Vorticity volume:*

At zero angle of attack the figures give a specific flow distribution which was not observed on previous models. At 6 degrees angle of attack the vorticity is well distributed and follows clearly the curvature of the wing tip. In comparison to the other models the trailing wake keeps its shape and volume with distance behind the wing

*Downwash effect:*

The geometry of this wing tip is not that of a typical winglet. In comparison to models B and C this configuration also improves the flow field and gives lower vertical position of the wake then model A.

### 3.4.2 Vector Plots of Velocity Distribution and Contour Plots of Vorticity Distribution

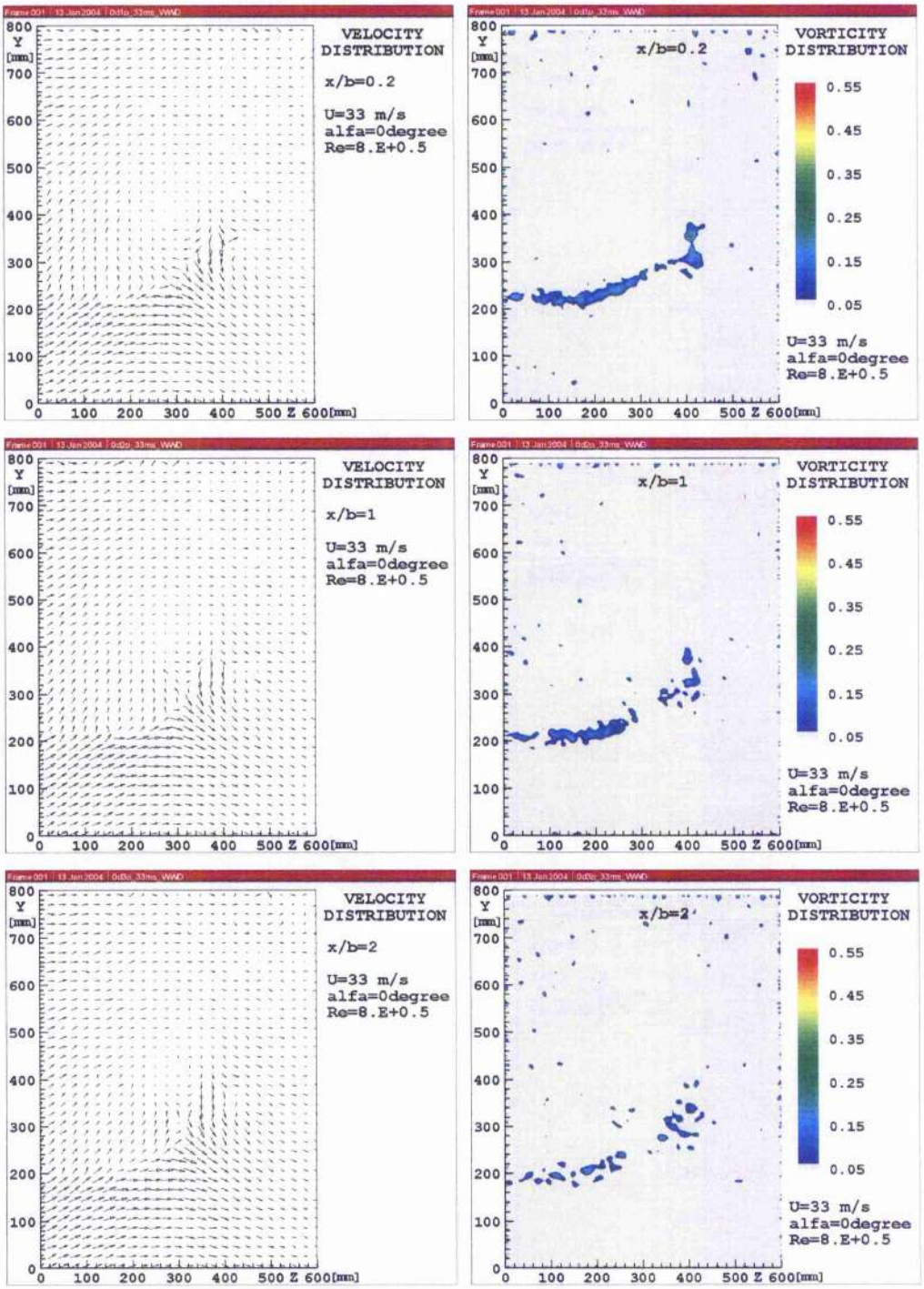


Figure 32. Velocity and vorticity distribution behind winglet **model D**, angle of attack **0 degrees**.

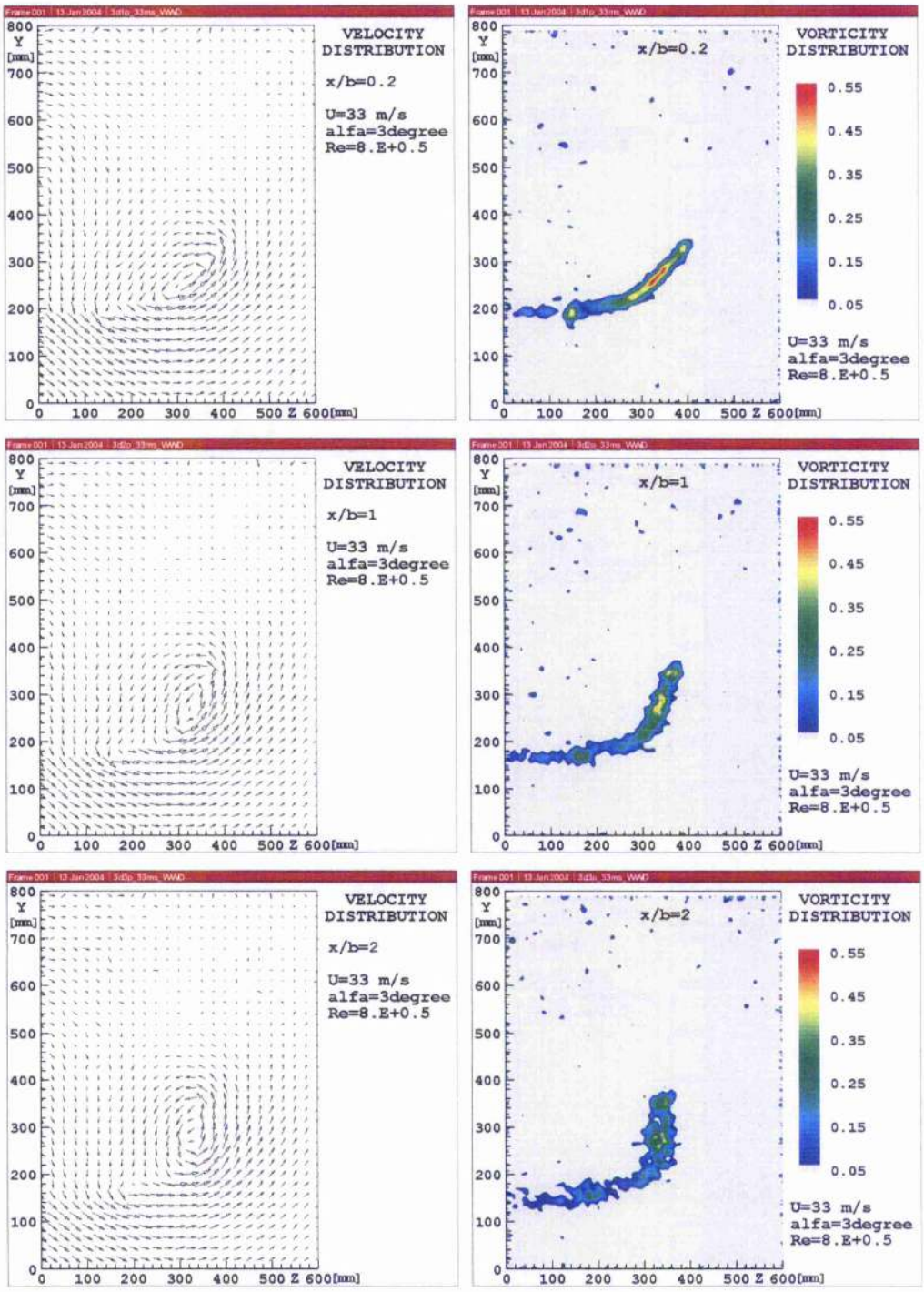


Figure 33. Velocity and vorticity distribution behind winglet **model D**, angle of attack **3 degrees**.

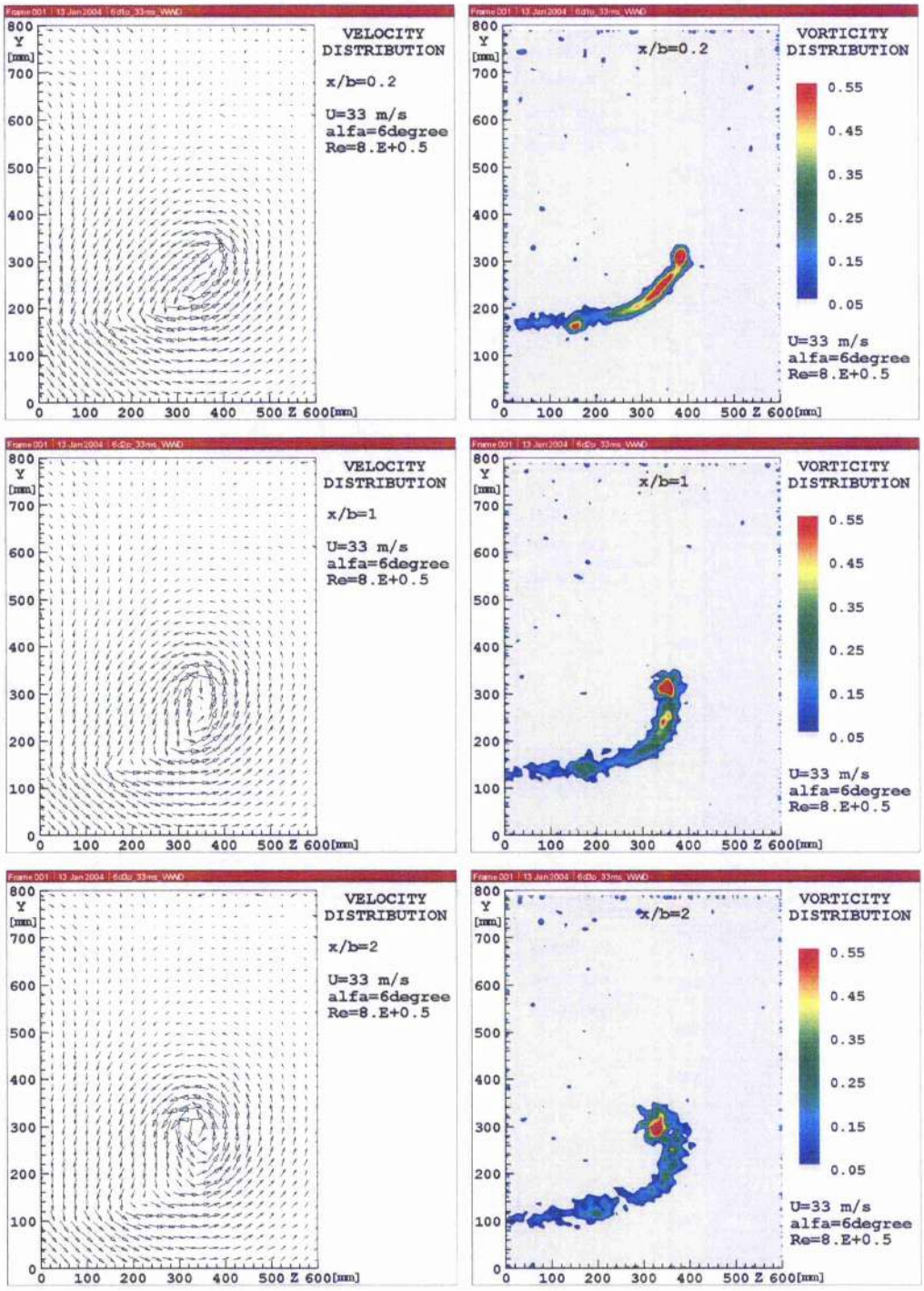


Figure 34. Velocity and vorticity distribution behind winglet **model D**, angle of attack **6 degrees**.

### 3.4.3 Downstream Wake Position

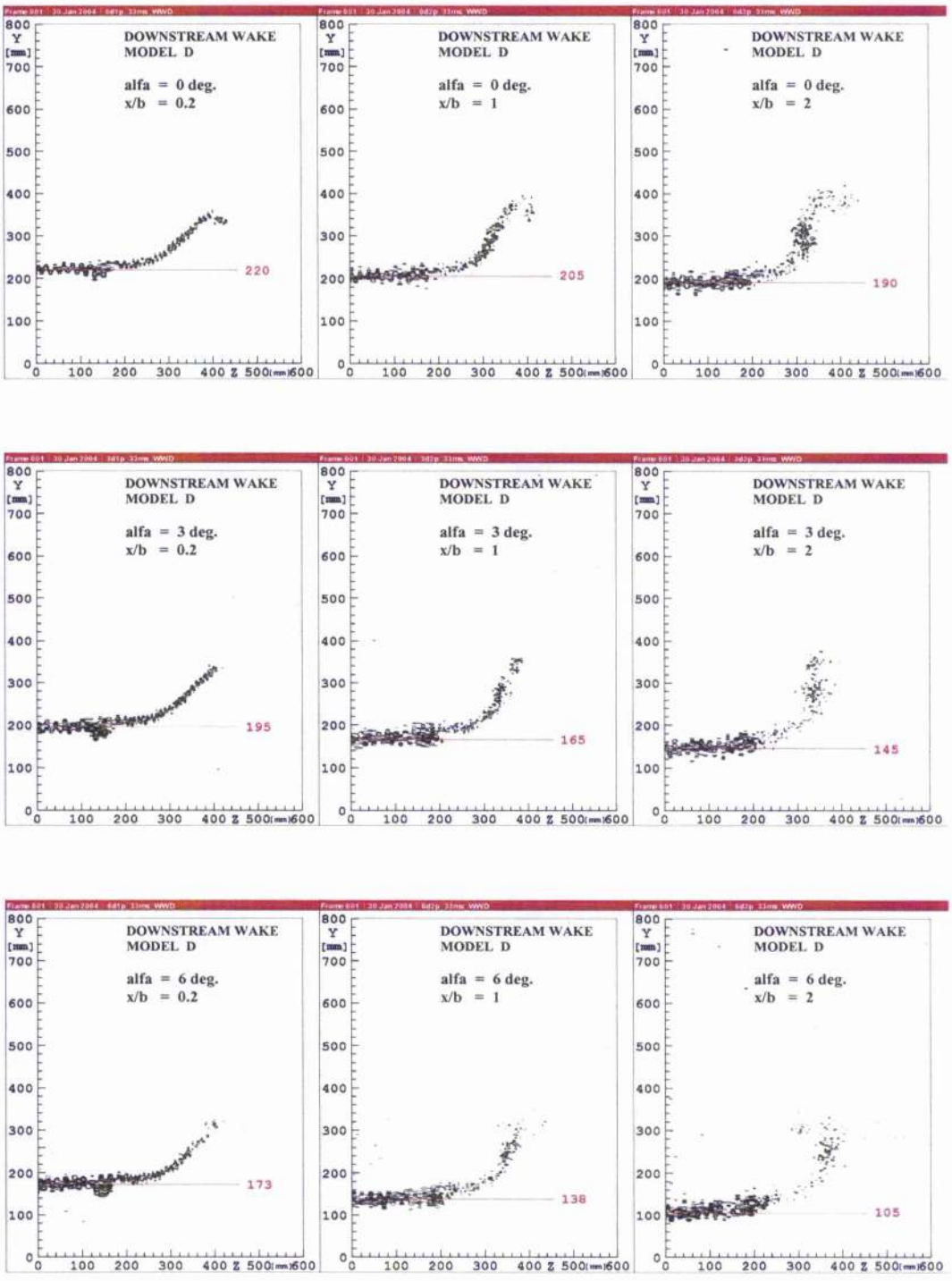


Figure 35. Downstream wake behind wing tip model D

# Chapter 4

## Analysis of the Results

### 4.1 Circulation: Definition and its Relation to Vorticity

This section describes the equations which have been used for the quantitative evaluation of the measured flow fields in terms of vorticity and circulation.

The circulation is defined as:

$$\Gamma = \oint_C u \cdot dl, \tag{4}$$

with the line integral taken along a closed contour C in a counter-clockwise sense (mathematical convention is that circulation is defined as numerically positive when counter-clockwise and negative when clockwise).

By using Stokes' theorem we can write equation (4) as a surface integral. If there is a finite value of circulation around C, then the fluid lying in any surface S bounded by C must include vorticity.

$$\oint_C u \cdot dl = \int_S (\nabla \cdot u) \cdot dS = \int_S \omega \cdot dS, \tag{5}$$

where the vorticity $\omega$ of the fluid is defined as

$$\omega = \nabla \times u \tag{6}$$

Physical meaning of vorticity: In two-dimensions, vorticity is the sum of angular velocities of any pair of mutually-perpendicular infinitesimal fluid lines passing through the point in question.

In other words, circulation is the integral counterpart of vorticity. This is Kelvin's circulation theorem, which states for inviscid (frictionless) fluids of uniform density with conservative forces that the circulation around a closed curve remains constant.

It is thus often necessary to define a vortex core where viscous forces are not negligible and the vorticity is finite and hence, there is a finite velocity. This rotational core can be idealized with a velocity profile (7)

$$u_\theta = 1/2 \cdot \omega_0 \cdot r_c/2, \tag{7}$$

where $r_c$ is the radius of the core. Matching velocities at $r = r_c$, this makes the flow irrotational outside the core (8)

$$u_\theta = 1/2 \cdot \omega_0 \cdot r_c^2/2r \tag{8}$$

and the circulation is defined as

$$\Gamma = \pi \cdot \omega_0 \cdot r_c^2 \tag{9}$$

This distribution, known as a Rankine vortex, has a region of constant vorticity at $r < r_c$ and a discontinuity at $r = r_c$, beyond which the vorticity is zero.

The vorticity field is calculated directly from the velocity field. Figure 36 shows the rectangular coordinate system for the measurement of a 3-dimensional velocity field, with +X in the direction of the freestream flow velocity, +Y normal to the plane of the wing, and +Z in the direction of the span of the wing.

Equation (10) determines the vorticity component along the X direction (streamwise vorticity), where V and W are the velocity components along Y and Z directions, respectively.

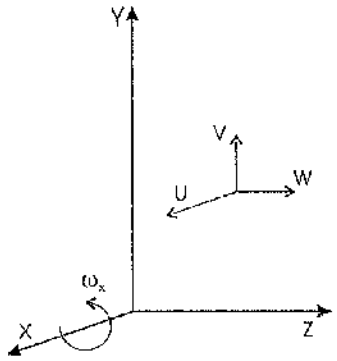


$$\omega_x = \frac{\partial V}{\partial z} - \frac{\partial W}{\partial y} \tag{10}$$

Figure 36. Coordinate system and velocity components definition

Figures 37 and 38 illustrate the calculation of the circulation in YZ plane behind the wing tip models based on equations (4) and (5):

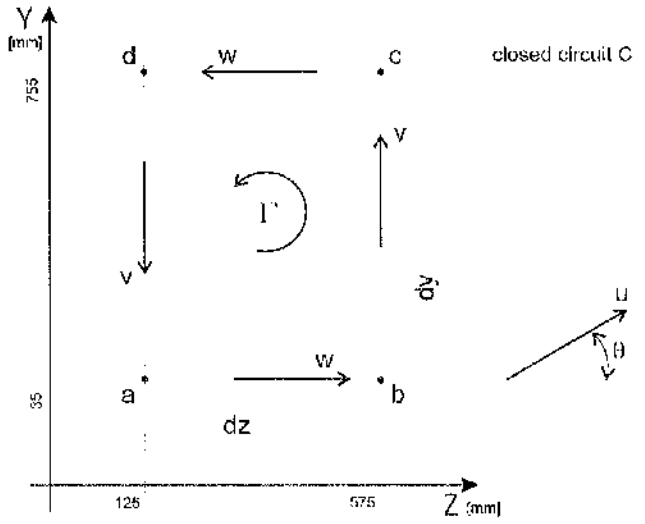


Figure 37. Definition of circulation in the YZ plane behind the wing tip models

The equation of circulation becomes

$$\Gamma = \oint_C \mathrm{u} \circ \mathrm{dl} = \oint_C \mathrm{u} \cdot \cos\theta \, \mathrm{dl} \qquad (11)$$

where the expression $\mathrm{u} \cdot \cos\theta$ is equal either to the vector **W** or **V** and **dl** is equal to the increment **dz** or **dy** (figure 37)

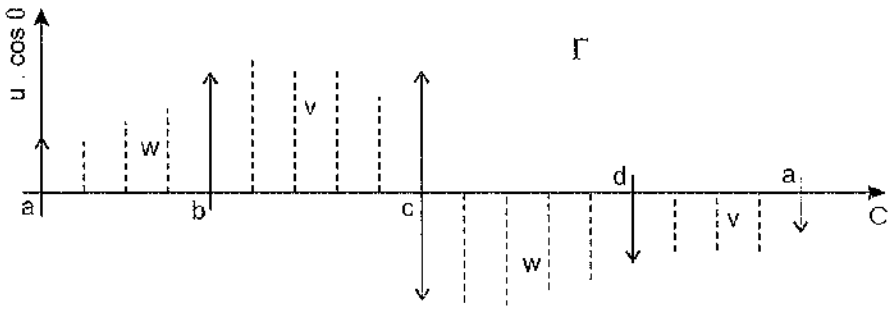


Figure 38. Vorticity area enclosed by the closed curve C

In this case vectors V and W were measured by a hot-wire probe. Using Simpson's formula for the calculation of limited integrals (figure 38) we can write equation (11) as

$$\begin{aligned}
\Gamma = & \int_a^b \left| \frac{h}{3}\left(w_0 + 4w_1 + 2w_2 + \ldots + 4w_{n-1} + w_n\right) \right| + \\
& + \int_b^c \left| \frac{h}{3}\left(v_0 + 4v_1 + 2v_2 + \ldots + 4v_{n-1} + v_n\right) \right| + \\
& + \int_c^d \left| \frac{h}{3}\left(w_0 + 4w_1 + 2w_2 + \ldots + 4w_{n-1} + w_n\right) \right| + \\
& + \int_d^a \left| \frac{h}{3}\left(v_0 + 4v_1 + 2v_2 + \ldots + 4v_{n-1} + v_n\right) \right| \quad [m^2/s] \qquad (12)
\end{aligned}$$

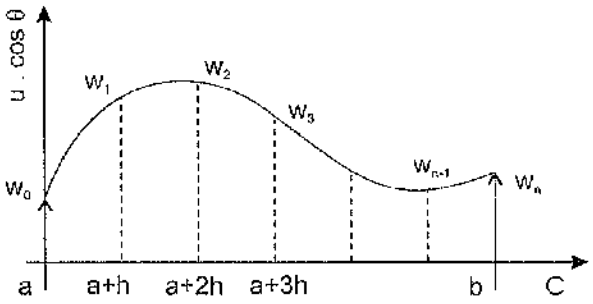


Figure 39. General function

where h = (b-a)/n = dz or dy (figure 37, 39)

The values of circulation have been calculated in all three downstream measurement planes (x/b=0.2, x/b=1, x/b=2).

## 4.2 Numerical Analysis of the Vorticity Distribution in terms of Circulation

The integral quantities calculated by the procedures given in the foregoing paragraph (4.1) are summarised in tables 2, 3, 4 and 5 in terms of the circulation magnitude.

The data included in the above tables, developed from figures 40, 41, 42 and 43, contain the calculated magnitude of circulation for a range of integration paths.

The contours (7 examples) along which the values of circulation have been calculated are shown in figures 40, 41, 42 and 43. The obvious requirement for the choice of the integration contour is a box that contains all the major vortex structures in all measured planes for all measured angles of attack. If the boxes contain all the vorticity then, theoretically, the magnitude of circulation should be constant regardless the path of integration.

The tables 2, 3, 4 and 5, give the calculated values for each of the contours, the average values of each measurement plane and the deviation of each contour from the average. In all causes the deviation stays within +- 5 % of the average.

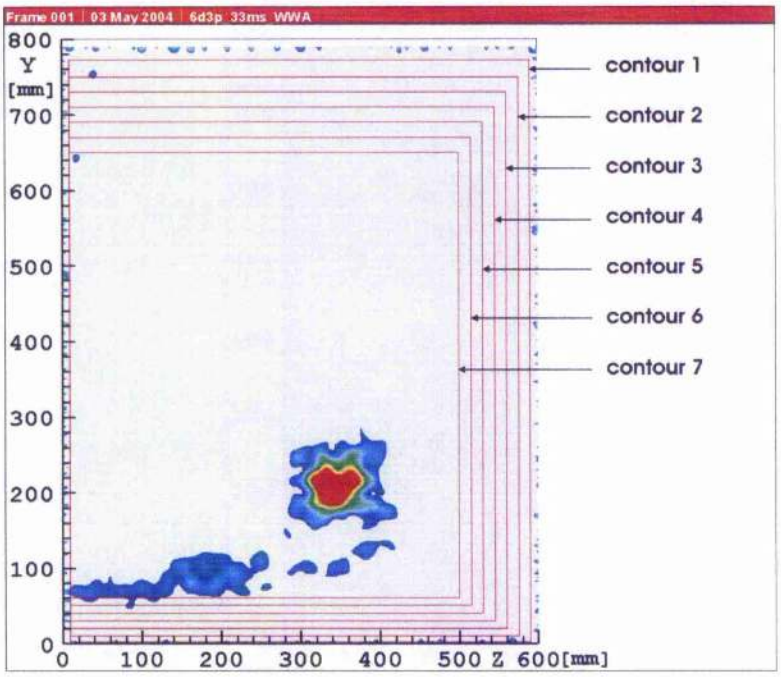


Figure 40. Definition of integration paths – model A

| **Contour No.:** | **Origin Z,Y:** | **Box dimension (Z, Y):** |
|---|---|---|
| Contour 1: | 10, 2.5 | 580, 770 |
| Contour 2: | 10, 10 | 565, 740 |
| Contour 3: | 10, 20 | 550, 710 |
| Contour 4: | 10, 30 | 535, 680 |
| Contour 5: | 10, 40 | 520, 650 |
| Contour 6: | 10, 50 | 505, 620 |
| Contour 7: | 10, 60 | 490, 590 |

Figure 40 shows the vorticity structure behind wing tip model A at an angle of attack of 3 degrees in the third measurement plane.

The integration paths have been chosen with respect to the vorticity structure so that even the smallest box still contains all the significant vortex structures.

| | deg. | 1 plane | | 2 plane | | 3 plane | |
|---|---|---|---|---|---|---|---|
| | | Γ [m²/s] * | | | | | |
| | 0 | 3161 | | 2900 | | 2862 | |
| | 3 | 3902 | | 3829 | | 3815 | |
| | 6 | 4877 | | 4853 | | 4807 | |
| | | | [%] ** | | [%*]* | | [%]** |
| contour 1: | 0 | 3184 | 1 | 2870 | 1 | 2892 | 1 |
| contour 2: | | 3180 | 1 | 2896 | 0 | 2778 | 3 |
| contour 3: | | 3184 | 1 | 2924 | 1 | 2875 | 0 |
| contour 4: | | 3183 | 1 | 2872 | 1 | 2855 | 0 |
| contour 5: | | 3200 | 1 | 2900 | 0 | 2858 | 0 |
| contour 6: | | 3099 | 2 | 2989 | 3 | 2877 | 1 |
| contour 7: | | 3100 | 2 | 2851 | 2 | 2900 | 1 |
| contour 1: | 3 | 3887 | 0 | 3845 | 0 | 3830 | 0 |
| contour 2: | | 3877 | 1 | 3710 | 3 | 3722 | 2 |
| contour 3: | | 3834 | 2 | 3873 | 1 | 3832 | 0 |
| contour 4: | | 3966 | 2 | 3797 | 1 | 3824 | 0 |
| contour 5: | | 3881 | 1 | 3771 | 2 | 3761 | 1 |
| contour 6: | | 4010 | 3 | 3932 | 3 | 3841 | 1 |
| contour 7: | | 3860 | 1 | 3877 | 1 | 3893 | 2 |
| contour 1: | 6 | 4881 | 0 | 4876 | 0 | 4788 | 0 |
| contour 2: | | 4749 | 3 | 4763 | 2 | 4711 | 2 |
| contour 3: | | 4918 | 1 | 4870 | 0 | 4847 | 1 |
| contour 4: | | 4876 | 0 | 4873 | 0 | 4804 | 0 |
| contour 5: | | 4892 | 0 | 4857 | 0 | 4870 | 1 |
| contour 6: | | 4883 | 0 | 4846 | 0 | 4868 | 1 |
| contour 7: | | 4940 | 1 | 4886 | 1 | 4762 | 1 |

* average value of circulation along 7 integrating contours
** deviation from the average value of circulation

Table 2. Dependence of the circulation magnitude on integration path for wing tip **model A**

Table 2 shows the circulation values calculated along 7 integration paths at angles of attack of 0, 3 and 6 degrees in three planes. The circulation values from 7 calculations are averaged and this average represents the total magnitude of circulation for the specific angle of attack and measurement plane.

The same procedure is used for the models B, C, D and the data are summarized in tables 3, 4 and 5.

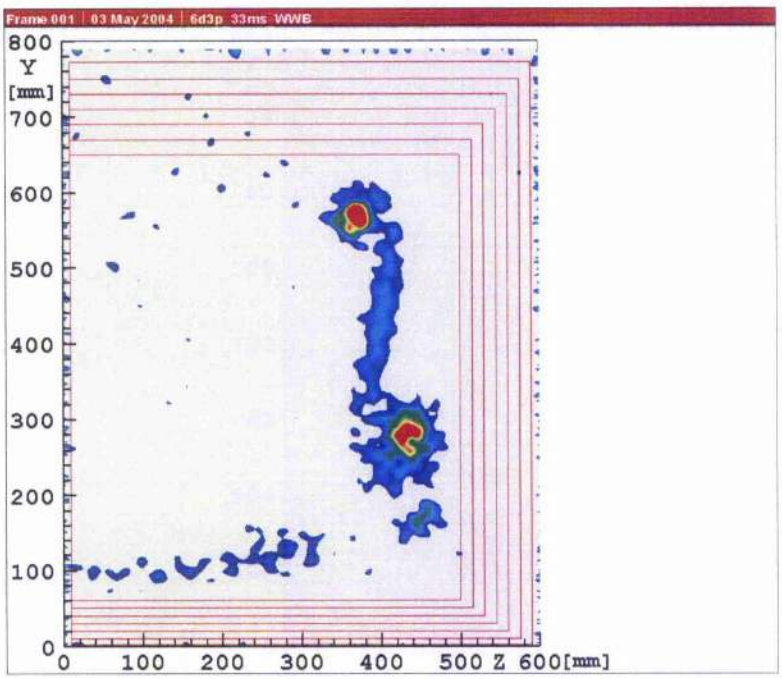


Figure 41. Definition of integrating paths – model B

| **Contour No.:** | **Origin Z,Y:** | **Box dimension (Z, Y):** |
|---|---|---|
| Contour 1: | 10, 2.5 | 580, 770 |
| Contour 2: | 10, 10 | 565, 740 |
| Contour 3: | 10, 20 | 550, 710 |
| Contour 4: | 10, 30 | 535, 680 |
| Contour 5: | 10, 40 | 520, 650 |
| Contour 6: | 10, 50 | 505, 620 |
| Contour 7: | 10, 60 | 490, 590 |

| | deg. | 1 plane | | 2 plane | | 3 plane | |
|---|---|---|---|---|---|---|---|
| | | $\Gamma$ [$m^2/s$] | | | | | |
| | -3 | 2320 | | 2063 | | 1995 | |
| | 0 | 2792 | | 2774 | | 2757 | |
| | 3 | 4308 | | 4263 | | 4122 | |
| | 6 | 5067 | | 5024 | | 4858 | |
| | | | [%] | | [%] | | [%] |
| Contour 1: | -3 | 2447 | 5 | 2073 | 0 | 2034 | 2 |
| Contour 2: | | 2440 | 5 | 2113 | 2 | 2088 | 5 |
| Contour 3: | | 2343 | 1 | 2095 | 2 | 2032 | 2 |
| Contour 4: | | 2325 | 0 | 2056 | 0 | 1948 | 2 |
| Contour 5: | | 2209 | 5 | 2047 | 1 | 1952 | 2 |
| Contour 6: | | 2247 | 3 | 2020 | 2 | 1973 | 1 |
| Contour 7: | | 2231 | 4 | 2037 | 1 | 1940 | 3 |
| Contour 1: | 0 | 2808 | 1 | 2798 | 1 | 2803 | 2 |
| Contour 2: | | 2661 | 5 | 2754 | 1 | 2660 | 4 |
| Contour 3: | | 2826 | 1 | 2828 | 2 | 2703 | 2 |
| Contour 4: | | 2779 | 0 | 2833 | 2 | 2808 | 2 |
| Contour 5: | | 2824 | 1 | 2716 | 2 | 2806 | 2 |
| Contour 6: | | 2773 | 1 | 2692 | 3 | 2763 | 0 |
| Contour 7: | | 2871 | 3 | 2795 | 1 | 2757 | 0 |
| Contour 1: | 3 | 4280 | 1 | 4272 | 0 | 4035 | 2 |
| Contour 2: | | 4124 | 4 | 4226 | 1 | 4002 | 3 |
| Contour 3: | | 4350 | 1 | 4201 | 1 | 4173 | 1 |
| Contour 4: | | 4394 | 2 | 4294 | 1 | 4041 | 2 |
| Contour 5: | | 4363 | 1 | 4329 | 2 | 4181 | 1 |
| Contour 6: | | 4248 | 1 | 4276 | 0 | 4230 | 3 |
| Contour 7: | | 4396 | 2 | 4246 | 0 | 4195 | 2 |
| | | | | | | | 100 |
| Contour 1: | 6 | 4990 | 2 | 5010 | 0 | 4801 | 1 |
| Contour 2: | | 4934 | 3 | 4916 | 2 | 4751 | 2 |
| Contour 3: | | 5052 | 0 | 5058 | 1 | 4907 | 1 |
| Contour 4: | | 5053 | 0 | 5106 | 2 | 4883 | 1 |
| Contour 5: | | 5115 | 1 | 5036 | 0 | 4844 | 0 |
| Contour 6: | | 5125 | 1 | 4998 | 1 | 4888 | 1 |
| Contour 7: | | 5200 | 3 | 5042 | 0 | 4932 | 2 |

Table 3. Dependence of the circulation magnitude on integration path for wing tip **model B**

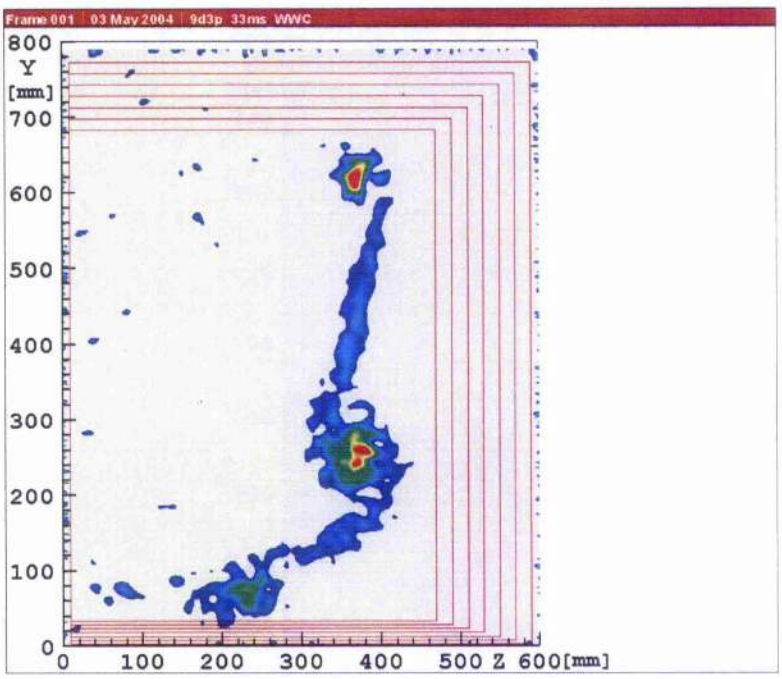


Figure 42. Definition of integrating paths – model C

| **Contour No.:** | **Origin Z,Y:** | **Box dimension (Z, Y):** |
|---|---|---|
| Contour 1: | 10, 2.5 | 580, 770 |
| Contour 2: | 10, 7.5 | 560, 750 |
| Contour 3: | 10, 12.5 | 540, 730 |
| Contour 4: | 10, 17.5 | 520, 710 |
| Contour 5: | 10, 22.5 | 500, 690 |
| Contour 6: | 10, 27.5 | 480, 670 |
| Contour 7: | 10, 32.5 | 460, 650 |

| | deg. | 1 plane | | 2 plane | | 3 plane | |
|---|---|---|---|---|---|---|---|
| | | Γ [m²/s] | | | | | |
| | -3 | 1621 | | 1555 | | 1542 | |
| | 0 | 2488 | | 2400 | | 2344 | |
| | 3 | 3182 | | 3159 | | 3130 | |
| | 6 | 4431 | | 4364 | | 4257 | |
| | 9 | 5203 | | 5118 | | 5095 | |
| | | | [%] | | [%] | | [%] |
| contour 1: | -3 | 1645 | 2 | 1613 | 4 | 1534 | 0 |
| contour 2: | | 1648 | 2 | 1579 | 2 | 1557 | 1 |
| contour 3: | | 1653 | 2 | 1521 | 2 | 1549 | 0 |
| contour 4: | | 1612 | 1 | 1559 | 0 | 1549 | 0 |
| contour 5: | | 1622 | 0 | 1564 | 1 | 1488 | 3 |
| contour 6: | | 1578 | 3 | 1552 | 0 | 1561 | 1 |
| contour 7: | | 1586 | 2 | 1500 | 4 | 1553 | 1 |
| contour 1: | 0 | 2501 | 1 | 2420 | 1 | 2339 | 0 |
| contour 2: | | 2573 | 3 | 2475 | 3 | 2433 | 4 |
| contour 3: | | 2559 | 3 | 2440 | 2 | 2405 | 3 |
| contour 4: | | 2452 | 1 | 2366 | 1 | 2324 | 1 |
| contour 5: | | 2482 | 0 | 2397 | 0 | 2303 | 2 |
| contour 6: | | 2445 | 2 | 2350 | 2 | 2306 | 2 |
| contour 7: | | 2401 | 3 | 2350 | 2 | 2298 | 2 |
| contour 1: | 3 | 3205 | 1 | 3198 | 1 | 3170 | 1 |
| contour 2: | | 3159 | 1 | 3139 | 1 | 3016 | 4 |
| contour 3: | | 3163 | 1 | 3145 | 0 | 3147 | 1 |
| contour 4: | | 3108 | 2 | 3104 | 2 | 3054 | 2 |
| contour 5: | | 3225 | 1 | 3170 | 0 | 3146 | 1 |
| contour 6: | | 3167 | 0 | 3155 | 0 | 3238 | 3 |
| contour 7: | | 3246 | 2 | 3200 | 1 | 3136 | 0 |
| contour 1: | 6 | 4442 | 0 | 4369 | 0 | 4297 | 1 |
| contour 2: | | 4313 | 3 | 4238 | 3 | 4227 | 1 |
| contour 3: | | 4406 | 1 | 4386 | 1 | 4319 | 1 |
| contour 4: | | 4469 | 1 | 4503 | 3 | 4306 | 1 |
| contour 5: | | 4468 | 1 | 4409 | 1 | 4255 | 0 |
| contour 6: | | 4441 | 0 | 4335 | 1 | 4266 | 0 |
| contour 7: | | 4481 | 1 | 4305 | 1 | 4127 | 3 |
| contour 1: | 9 | 5181 | 0 | 5144 | 1 | 5027 | 1 |
| contour 2: | | 5075 | 2 | 5098 | 0 | 5011 | 2 |
| contour 3: | | 5188 | 0 | 5227 | 2 | 5061 | 1 |
| contour 4: | | 5263 | 1 | 5117 | 0 | 5083 | 0 |
| contour 5: | | 5217 | 0 | 5229 | 2 | 5134 | 1 |
| contour 6: | | 5191 | 0 | 5036 | 2 | 5225 | 3 |
| contour 7: | | 5303 | 2 | 4972 | 3 | 5127 | 1 |

Table 4. Dependence of the circulation magnitude on integration path for wing tip **model C**

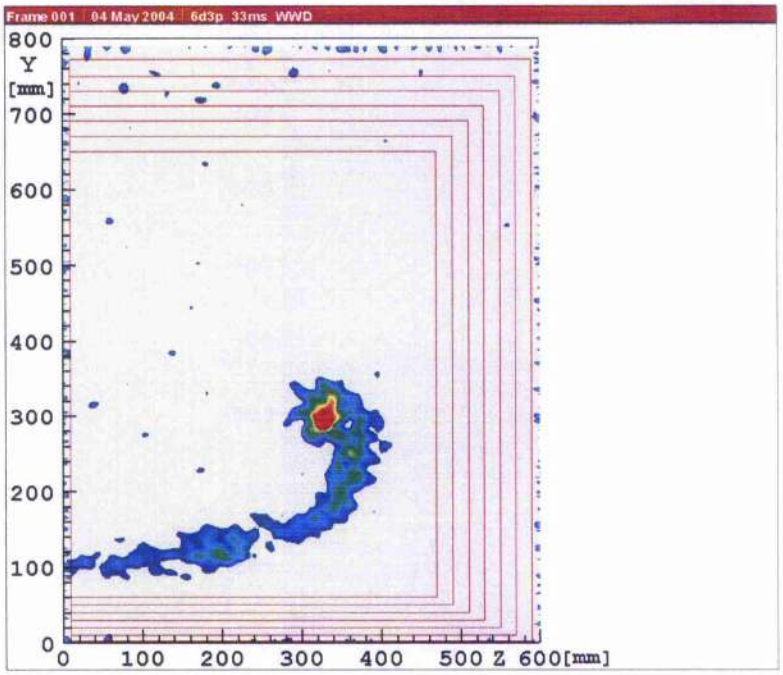


Figure 43. Definition of integrating paths – model D

| **Contour No.:** | **Origin Z,Y:** | **Box dimension (Z, Y):** |
|---|---|---|
| Contour 1: | 10, 2.5 | 580, 770 |
| Contour 2: | 10, 10 | 560, 740 |
| Contour 3: | 10, 20 | 540, 710 |
| Contour 4: | 10, 30 | 520, 680 |
| Contour 5: | 10, 40 | 500, 650 |
| Contour 6: | 10, 50 | 480, 620 |
| Contour 7: | 10, 60 | 460, 590 |

| | deg. | 1 plane | | 2 plane | | 3 plane | |
|---|---|---|---|---|---|---|---|
| | | Γ [m²/s] | | | | | |
| | 0 | 2694 | | 2516 | | 2485 | |
| | 3 | 3318 | | 3269 | | 3259 | |
| | 6 | 4041 | | 3950 | | 3907 | |
| | | | [%] | | [%] | | [%] |
| contour 1: | 0 | 2685 | 0 | 2582 | 3 | 2548 | 3 |
| contour 2: | | 2608 | 3 | 2538 | 1 | 2476 | 0 |
| contour 3: | | 2753 | 2 | 2584 | 3 | 2510 | 1 |
| contour 4: | | 2660 | 1 | 2445 | 3 | 2510 | 1 |
| contour 5: | | 2660 | 1 | 2492 | 1 | 2453 | 1 |
| contour 6: | | 2734 | 1 | 2527 | 0 | 2417 | 3 |
| contour 7: | | 2757 | 2 | 2442 | 3 | 2484 | 0 |
| | | | | | | | |
| contour 1: | 3 | 3397 | 2 | 3231 | 1 | 3322 | 2 |
| contour 2: | | 3258 | 2 | 3151 | 4 | 3205 | 2 |
| contour 3: | | 3337 | 1 | 3217 | 2 | 3281 | 1 |
| contour 4: | | 3263 | 2 | 3298 | 1 | 3238 | 1 |
| contour 5: | | 3290 | 1 | 3333 | 2 | 3299 | 1 |
| contour 6: | | 3347 | 1 | 3315 | 1 | 3254 | 0 |
| contour 7: | | 3337 | 1 | 3336 | 2 | 3217 | 1 |
| | | | | | | | |
| contour 1: | 6 | 4112 | 2 | 3911 | 1 | 3949 | 1 |
| contour 2: | | 3938 | 3 | 3815 | 3 | 3846 | 2 |
| contour 3: | | 4032 | 0 | 4020 | 2 | 3894 | 0 |
| contour 4: | | 4087 | 1 | 3914 | 1 | 3933 | 1 |
| contour 5: | | 4028 | 0 | 4021 | 2 | 3951 | 1 |
| contour 6: | | 4069 | 1 | 3948 | 0 | 3894 | 0 |
| contour 7: | | 4022 | 1 | 4021 | 2 | 3883 | 1 |

Table 5. Dependence of the circulation magnitude on integration path for wing tip **model D**

## 4.3 The Discussion of Experimental Results

Plots which summarize the analysis of circulation and the location of the wake are presented in figures 44, 45, 46, 47, 48, 49 and 50.

The plots of circulation (figures 44, 45, 46, 47 and 48) are given in terms of circulation as a dimensional value [$m^2$/sec] and consequently relate to the lift force [N], not to the lift coefficient. The differences in the magnitude of circulation for the particular models are therefore due, in parts, to different wing tip areas and so preclude the direct comparison on a dimensional basis.

The measured models represent four wing tip geometries. Their spans are identical but, due to the different planforms, the four wing tips do not have the same aspect ratio. As a consequence, direct comparison of the details of the flow can't be made. Due to the planform similarity, however, it is possible to make a qualitative comparison between models A and B and to same extent between models C and D.

It should be noted that a series of experiments based on the four wing tips is not sufficient to completely describe and understand the complexity of vortex systems downstream the wing. Despite these limitations some observations arising from the measurements can be made.

1. Lift is proportional to circulation (the Law of Kutta-Joukovski). A consequence of this is that the variation of circulation against angle of attack within the linear range of lift should also be linear. The measurements are in accord with this statement only in the case of models A, D and partially C. The deviation in figure 45 (model B) is assumed to be due to the contribution of the winglet to the total measured circulation.

2. Not withstanding point 1 above, the direct contribution of the winglets to the wing lift is generally of a small order, so that the total value of circulation is expected not to be significantly different from model to model. The comparisons of data for the wing tips (A-B) and (C-D) show differences in the magnitude of circulation which are not substantial (figure 48).

3. The theory of vorticity concludes that the intensity of circulation in an ideal flow field should stay constant along the vortex structures downstream the wing. Obviously in real flow fields the circulation reduces at increasing distances owing to friction and energy dissipation. The distances of the measurement planes behind the wing are not enough to observe a significant circulation decrease (figures 44, 45, 46, 47). The planes where the cross flow was measured are still in a wing near field so that the decrease is not too pronounced. Despite this, a gradual reduction is observed in all cases.

4. The measurements of downwash clearly show that the difference in the vertical downwash location is significantly reduced (weaker downwash) when the winglet is incorporated (model A - B, Figure 49). It indicates smaller induced values along the wing span which consequently lead to the reduction of the induced drag. The decrease of the vertical position of downwash is of the value (15-20) %. It should be noted that there is no simple correspondence between the downwash and the induced drag. Despite that the measurements indicate that even when the magnitude of total circulation is not changed the winglets and their geometry alter significantly the form and position of downwash affecting thus the induced drag.

The above remarks are consistent with the theory relevant to the development of vortex structures in the flow field downstream the wing.

Direct comparison of the models has been impeded by their geometry which is not of the same aspect ratio. For evaluating induced quantities this parameter is the most important. Any further research on the problem should avoid this shortcoming by preparing of models of the same aspect ratio and, moreover, of a larger semi-span.

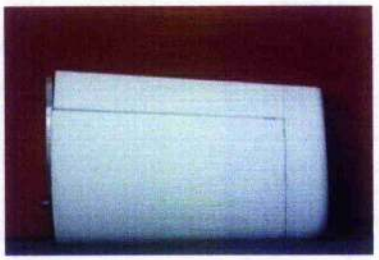

| Winglet model A | Γ [m²/s] | | | |
|---|---|---|---|---|
| | | 1st xy plane | 2nd xy plane | 3rd xy plane |
| | alfa = 0 degree | **3161** | **2900** | **2862** |
| | alfa = 3 degrees | **3902** | **3829** | **3815** |
| | alfa = 6 degrees | **4877** | **4853** | **4807** |

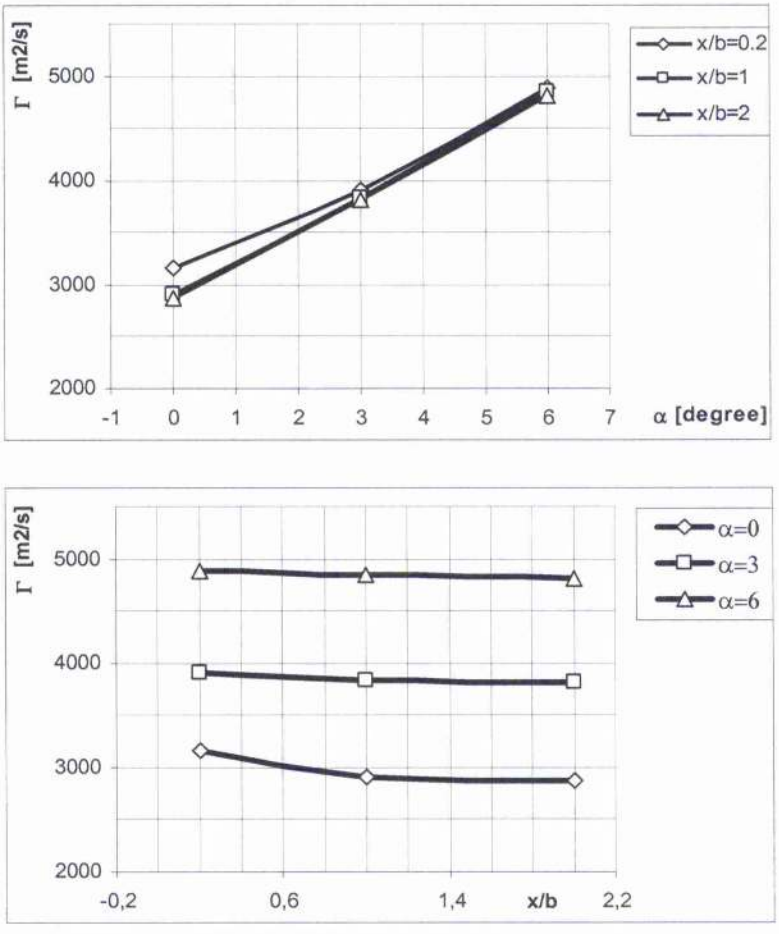


Figure 44. Circulation behind wing tip model A

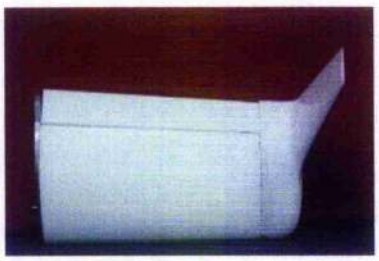

| Winglet model B | Γ [m²/s] | | | |
|---|---|---|---|---|
| | | 1st xy plane | 2nd xy plane | 3rd xy plane |
| | alfa = - 3 degrees | **2320** | **2063** | **1995** |
| | alfa = 0 degree | **2792** | **2774** | **2757** |
| | alfa = 3 degrees | **4308** | **4263** | **4122** |
| | alfa = 6 degrees | **5067** | **5024** | **4858** |

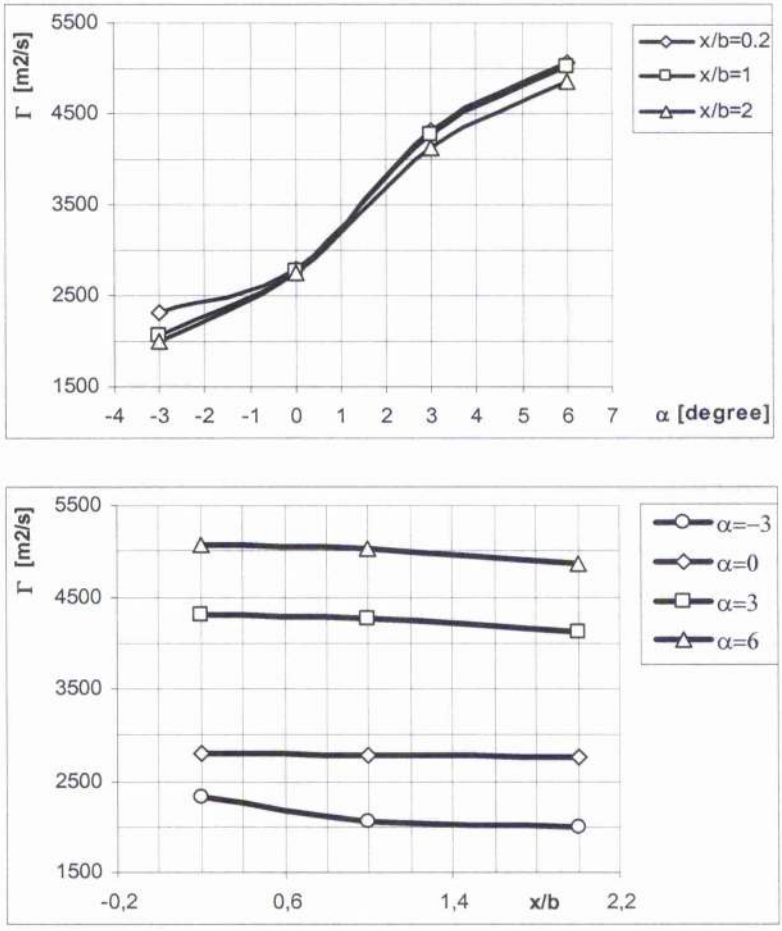


Figure 45. Circulation behind winglet model B

| Winglet model C | Γ [m²/s] | | | |
|---|---|---|---|---|
| | | 1st xy plane | 2nd xy plane | 3rd xy plane |
| | alfa = - 3 degrees | **1621** | **1555** | **1542** |
| | alfa = 0 degree | **2488** | **2400** | **2344** |
| | alfa = 3 degrees | **3182** | **3159** | **3130** |
| | alfa = 6 degrees | **4431** | **4364** | **4257** |
| | alfa = 9 degrees | **5203** | **5118** | **5095** |

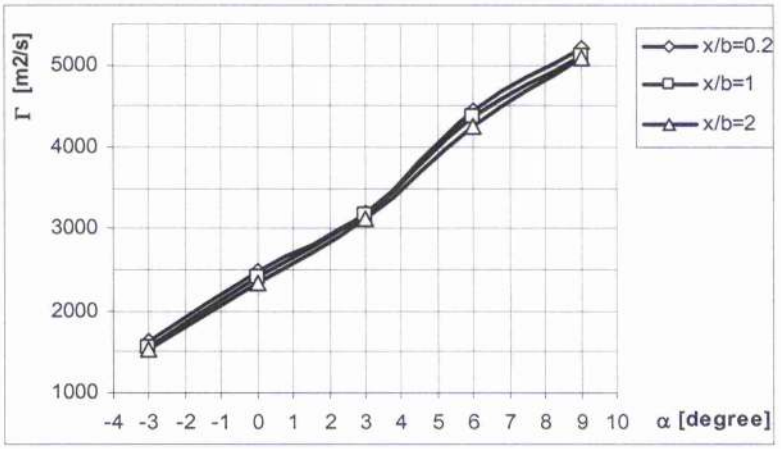


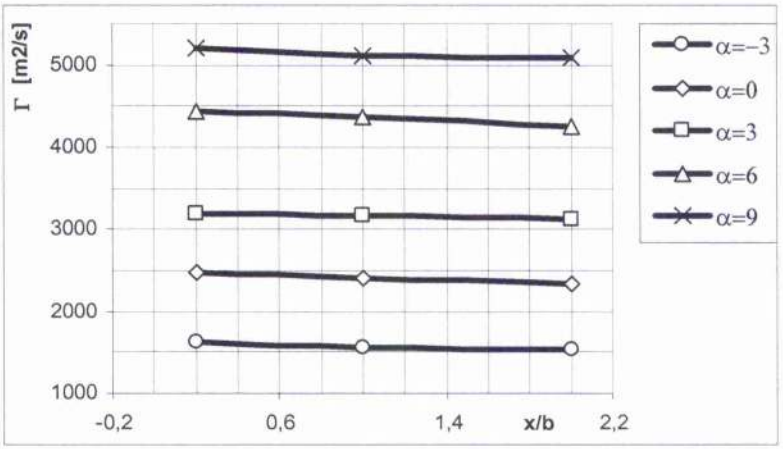


Figure 46. Circulation behind winglet model C

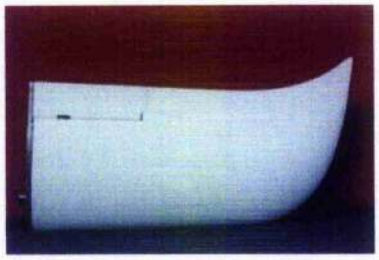

| Winglet model D | Γ [m²/s] | | | |
|---|---|---|---|---|
| | | 1st xy plane | 2nd xy plane | 3rd xy plane |
| | alfa = 0 degree | **2694** | **2516** | **2485** |
| | alfa = 3 degrees | **3318** | **3269** | **3259** |
| | alfa = 6 degrees | **4041** | **3950** | **3907** |

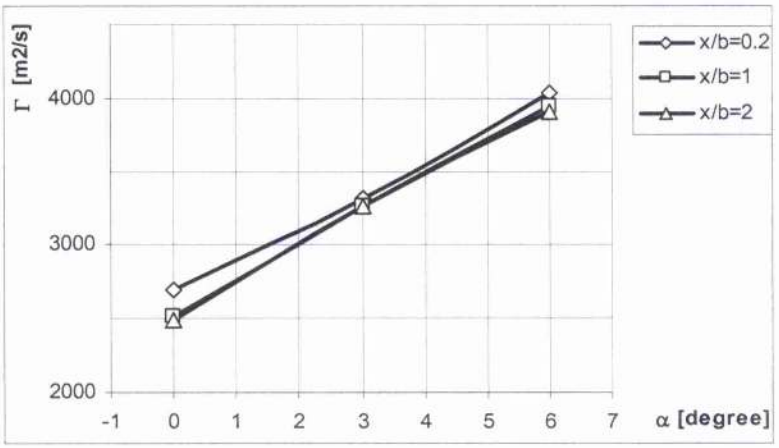


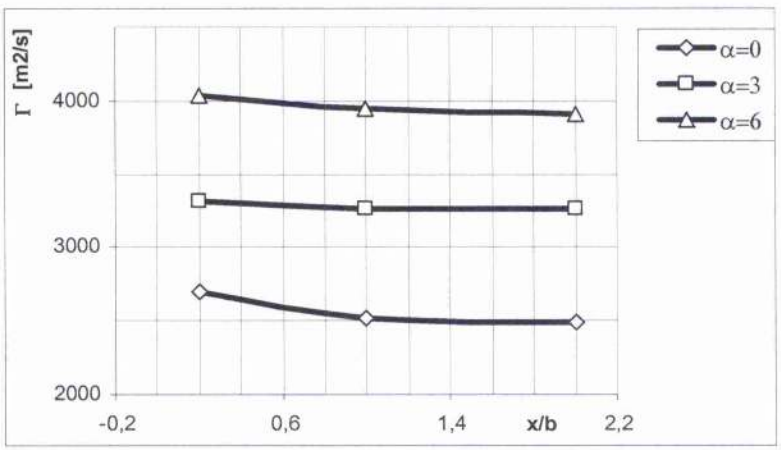


Figure 47. Circulation behind wing tip model D

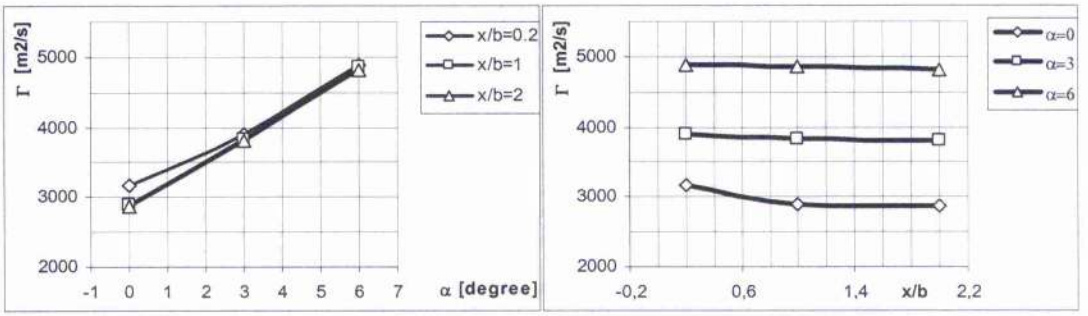


wing tip model A

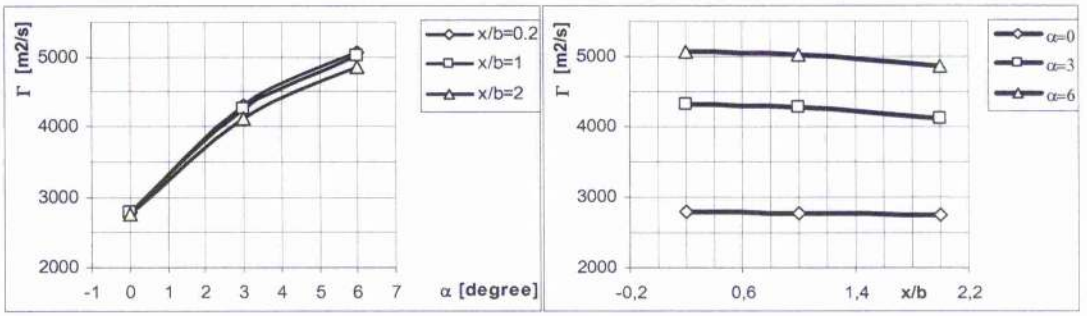


winglet model B

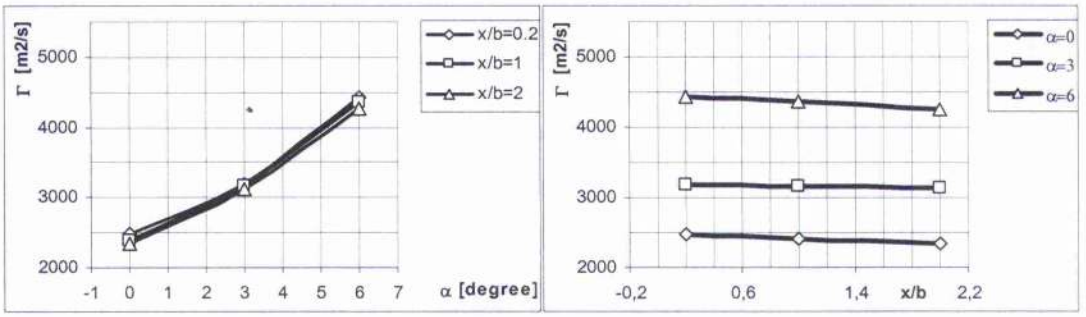


winglet model C

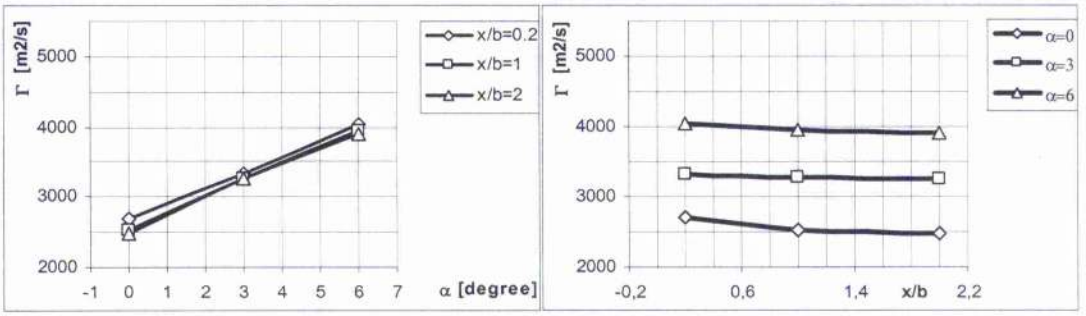


wing tip model D

Figure 48. Summary of circulation behind wing tip models

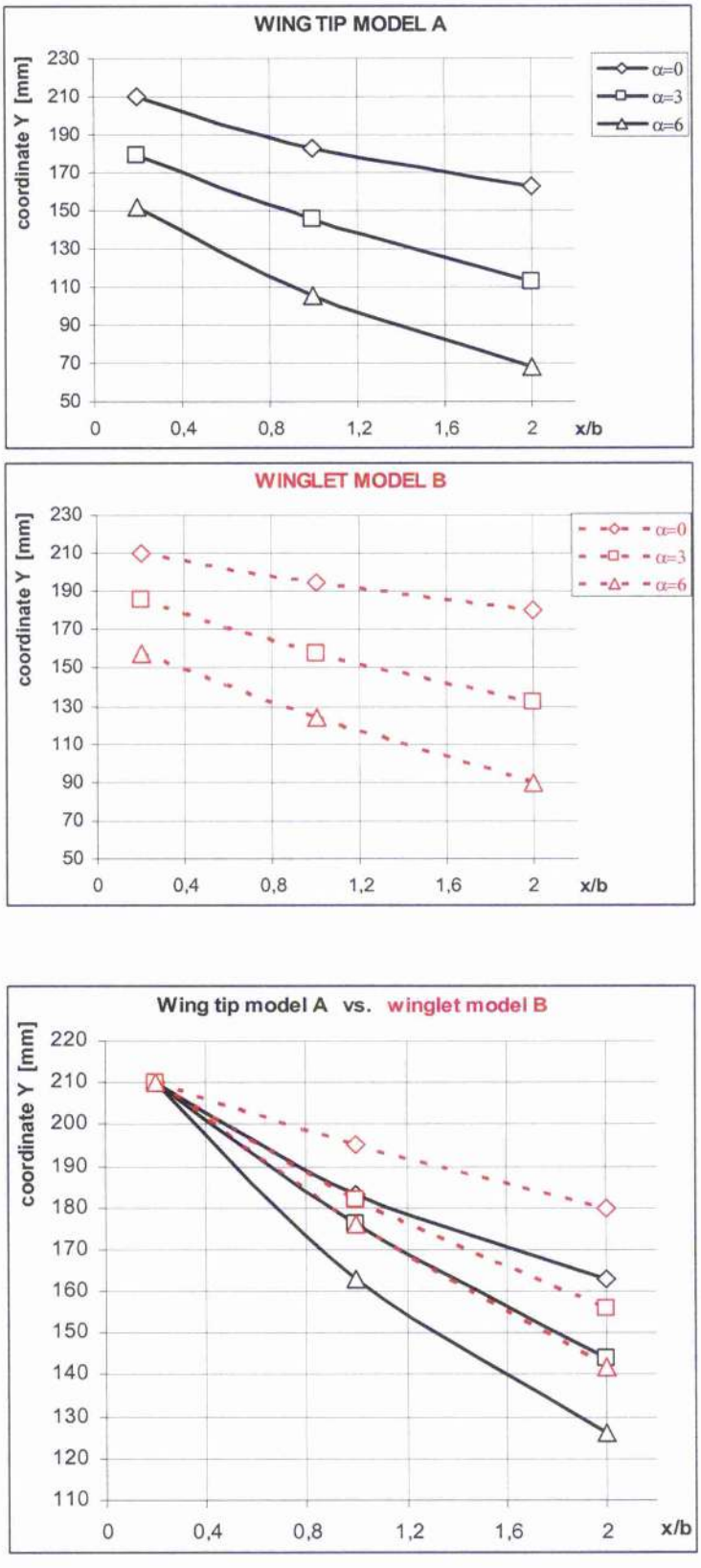


Figure 49. Downstream wake position behind wing tip model A vs. winglet model B

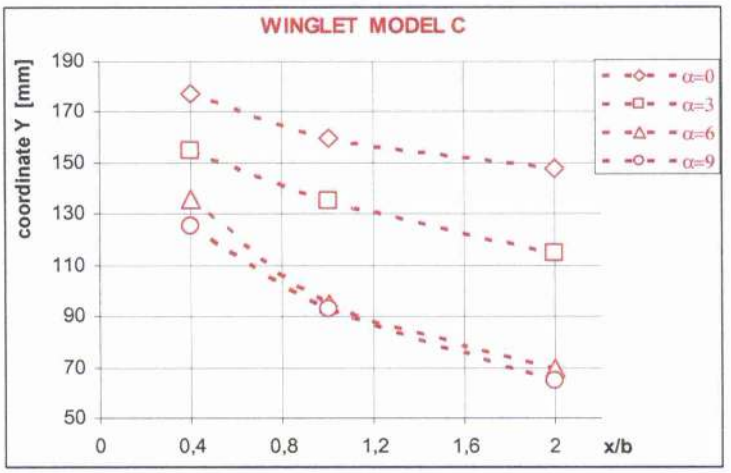


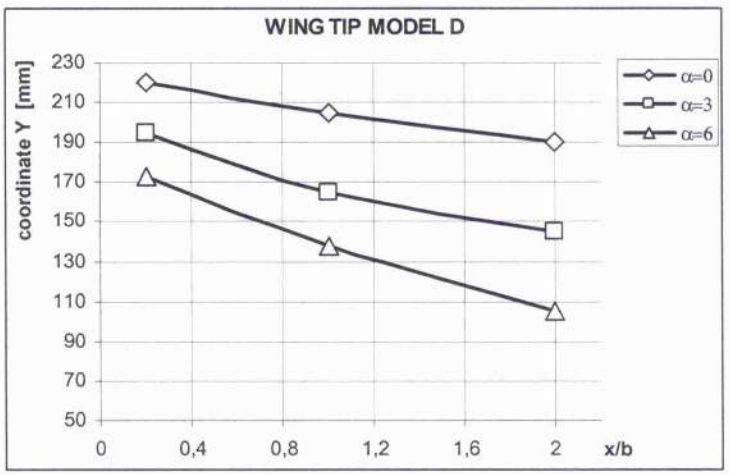


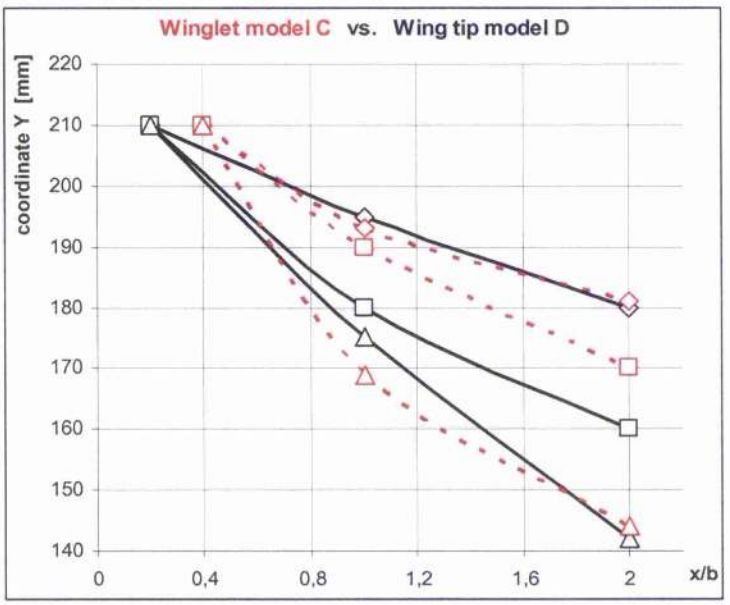


Figure 50. Downstream wake position behind winglet model C vs. wing tip model D

# Chapter 5

## Conclusion

Experimental instrumentation for the investigation of the flow field behind wing tip models has been designed, manufactured and set-up. A newly designed traverse mechanism has made it possible for measurements to be made at high spatial resolution within a large enough area for full size wing tip models to be tested. An additional feature of the system is that the time required for testing is also relatively short, depending on the grid size and the number of planes. Complete mapping may be done in a couple of hours, covering the full size wing tip model, several angles of attack and a fine testing grid size.

The experimental results that have been collected in this project demonstrate first of all the feasibility of mapping 3-D flow fields with the CTA anemometer. The examples show how data can be exported and presented in 3-D vector and contour plots. The combined vector/contour plots for a system of testing planes behind the models may also indicate how the wing tip vortices behave and develop with increased distance from the wing.

The experimental investigations clearly indicate that at the comparable values of the total wing circulation (wing lift) the winglet geometry influences the character and the position of induced flow quantities. In particular, both the vorticity distribution and downwash are altered in a manner that will have a direct impact on the wing induced drag.

The analysis of experimental results concludes that the measured data comply with the physical image of vortex structures which is expected to develop downstream the wing.

The work carried out here confirms the importance of the investigated phenomena on the induced flow around the wing and should serve as the preparation for further systematic research.

# Appendix A

## Hot Wire Anemometry and Concept of Effective Velocity

## Cross-Wire Sensor and Concept of Effective Velocity

The Cross-Wire Sensor combines two hot wires in the plane to form a 'X'. The X-wire sensor analysis makes the assumption that the velocity is in the plane of the two sensors (Figure 51.). The sensor inclination angle (slant) is the angle measured in the plane of the needles made by a sensor with the normal to the probe axis. The nominal slant angle for a cross-wire sensor probe is 45 degrees. The dimensions of the sensor's wires are 0.005 mm in diameter and 1.25 mm long. The total measurement volume is approximately 0.5 $mm^3$. The wire material is platinum plated tungsten. The probe holder keeps the sensor wires 45 mm upstream of the main part of the probe.

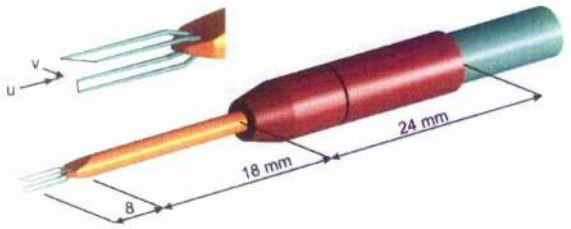


Figure 51. X-wire sensor Dantec 55P51

To define a relationship between the sensor's output voltage and velocity that is independent of orientation, the concept of effective velocity shall be explained. Several cooling 'laws' have been proposed to introduce the effective cooling velocity.


Figure 52. Illustration of the effective velocity

The example given above is referred to as the Cosine law (Figure 52), where

$$V_{eff} = \hat{V} \cdot \cos\alpha \tag{13}$$

Since the heat loss of the wire is not zero at alpha equals ninety degrees the cosine relationship does not hold. A more accurate description of the directional sensitivity of inclined sensors is given by Jorgensen's equation:

$$V_{eff}^2 = \hat{V}^2\left[\cos^2\alpha + k^2\sin^2\alpha\right] \tag{14}$$

where $k$ is the calibration constant found empirically.

The equation (14) can be rewritten in terms of velocity vectors with respect to the sensor geometry:

$$V_{eff}^2 = U_N^2 + k * U_T^2 \tag{15}$$

Referring to Jorgensen's equation and rewriting it for the two sensors in a cross-wire sensor probe (Fig. 47) we obtain (15) or (16) and since $U_{N1} = U_{T2}$ and $U_{T1} = U_{N2}$

$$V_{eff2}^2 = U_{N2}^2 + k_2^2 * U_{T2}^2 = U_{T1}^2 + k_2^2 * U_{N1}^2 \tag{16}$$

$$U_{N1}^2 = \frac{V_{eff1}^2 - k_1^2 * V_{eff2}^2}{1 - k_1^2 * k_2^2} \tag{17}$$

$$U_{T1}^2 = \frac{V_{eff2}^2 - k_2^2 * V_{eff1}^2}{1 - k_1^2 * k_2^2} \tag{18}$$

Hence, given a pair of cooling velocities ($V_{eff1}$, $V_{eff2}$) from a single measurement of a cross-wire sensor probe, we can compute the $u$ and $v$ components and also the total magnitude $\hat{V}$.

$$U = \frac{U_{N1} + U_{T1}}{\sqrt{2}} \tag{19}$$

$$V = \frac{U_{N1} - U_{T1}}{\sqrt{2}} \tag{20}$$

$$\hat{V} = \left(U^2 + V^2\right)^{1/2} \tag{21}$$

## Converting Voltage to Effective Velocity

Each of the sensor wires is handled by using the TSI IFA 300 constant Temperature Unit. The correlation between the output voltage and cooling velocities is obtained according to King's Law

$$E = A + B \cdot V_{eff}^{N} \tag{22}$$

where, $E$ is the voltage across the wire, $V_{eff}$ is the velocity of the flow normal to the wire and $A$, $B$ and $N$ are constants. $A$ can be found by measuring the voltage on the hot wire with no flow. Once we know $A$ we can measure the wire voltage for a known flow velocity and then determine $B$ from King's Law, $N$ =0.45 is common for hot-wire probes.

The basic output of the anemometer is called the bridge voltage, $E_b$. This voltage is signal conditioned, $E_0$, in order to obtain the optimum resolution of the A/D converter:

$$E_0 = (E_b - Ofset) \times Gain \tag{23}$$

The temperature corrected voltage, $E$, is then calculated as follows:

$$E = E_b \times \sqrt{\frac{(T_s - T_c)}{(T_s - T_a)}} \tag{24}$$

The basic calibration is a curve fit to the effective velocity, $V_{eff}$, as a function of the bridge voltage, $E$, where:

$$V_{eff} = K + A \times E + B \times E^2 + C \times E^3 + D \times E^4 \tag{25}$$

Then density correction is applied as follows:

$$V_{eff(cor)} = \frac{P_c}{P} \times V_{eff} \tag{26}$$

Where:

$P_c$ = Atmospheric Pressure during calibration

$P$ = Atmospheric Pressure during test

The temperature and density corrections are derived from a form of "King's Law" as follows:

$$\frac{E_b^2}{(T_s - T)} = A' + B' \times (P \times V_{eff})^{1/N} \tag{27}$$

## X-Wire Sensor Calibration

The X-wire sensor must be placed in the uniform jet to obtain the correlation between the output voltage and cooling velocities according to King's Law.

By placing the x-wire in the jet and maneuvering it to all the possible flow angle combinations according to the figure (53), the yaw angle calibration is performed. The relation between cooling velocities and flow angles is determined by comparing the known yaw angles and known velocity.

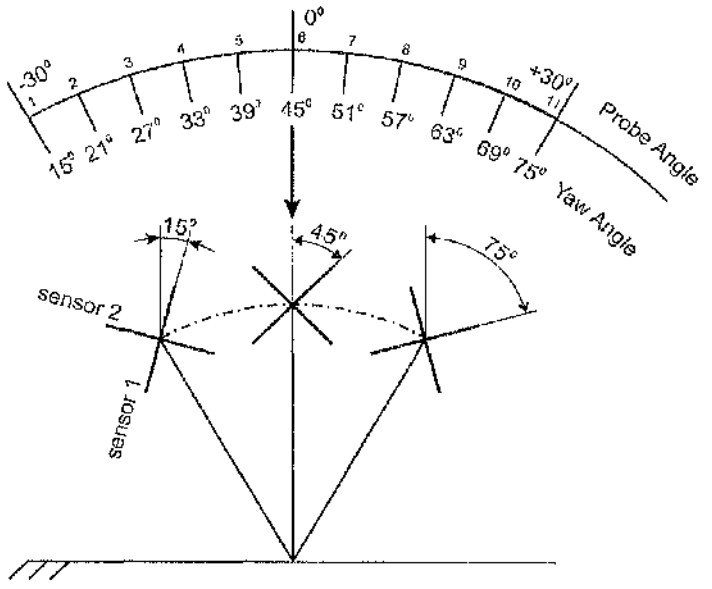


Figure 53. Probe positions and yaw angle calibration of the X-wire sensor

Figure 54 shows specific values of the Bridge Voltage obtained during calibration procedure for the velocity range 0 – 41 m/s. The result of the correlation between the velocity and voltage is shown in figure 55.

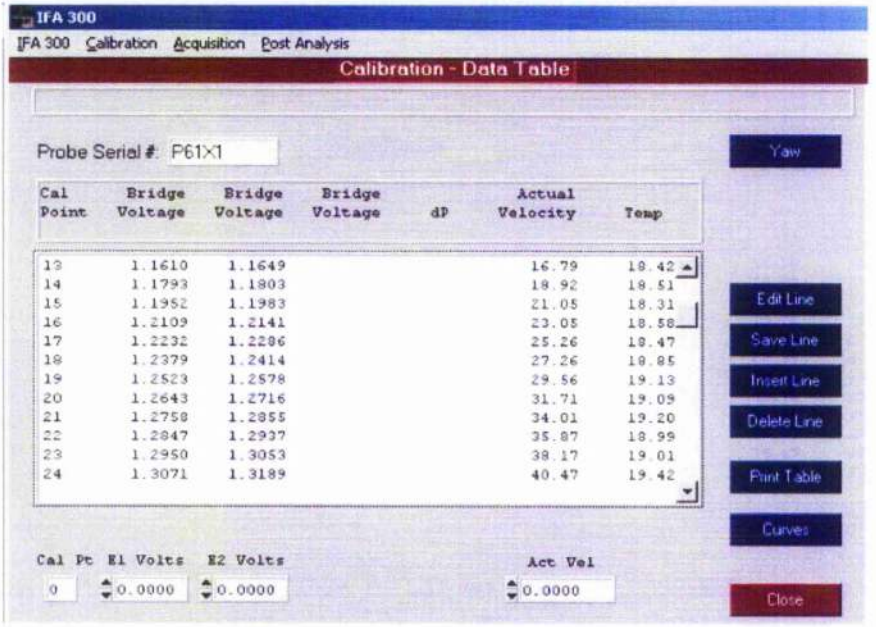


Figure 54. Data table - voltage vs. velocity

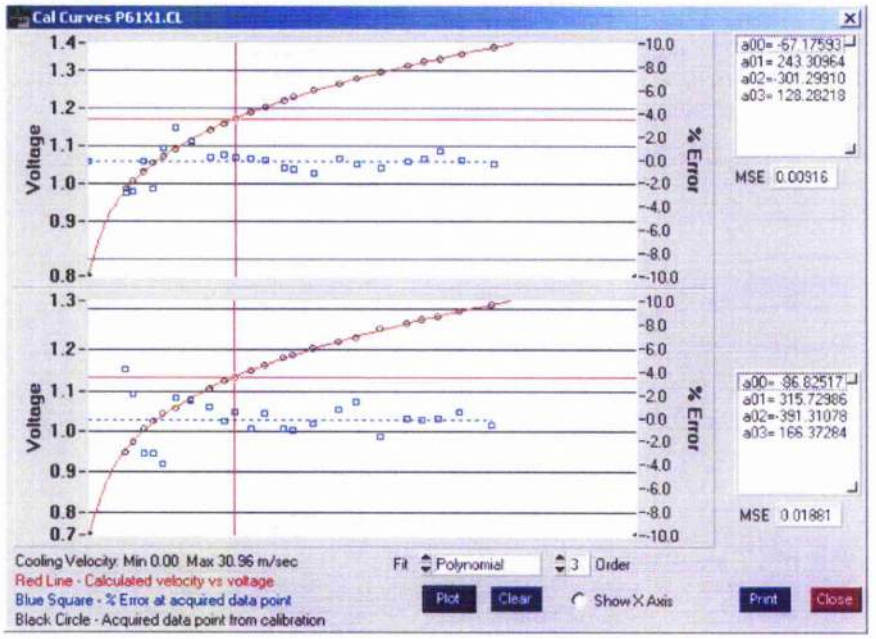


Figure 55. The x-wire sensor specific calibration curves

Figure 56 shows the relation between the Yaw Angle and Bridge Voltage for probe positioning given in figure 53.

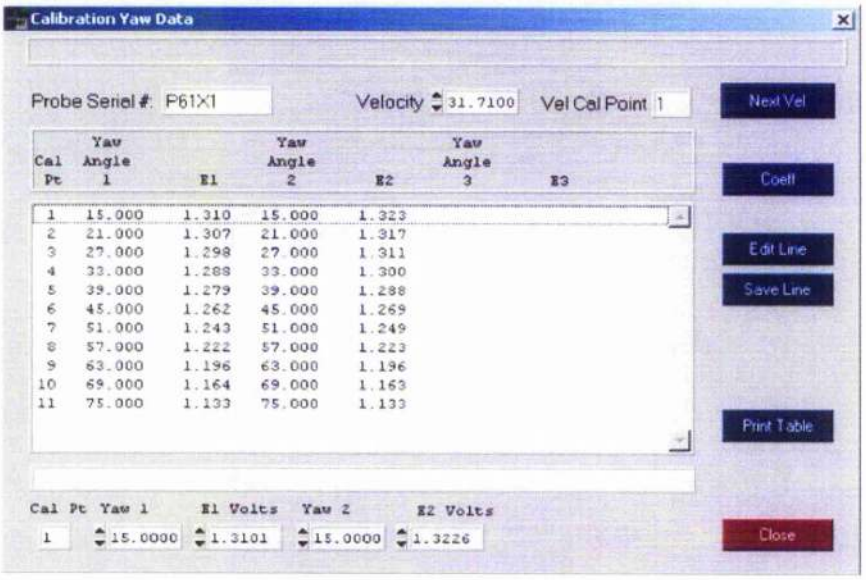


Figure 56. The yaw angle calibration table

# References


Allen, J.G., "Vortex Drag Reduction Using Wing Tip Sails," Thesis, Cranfield Institute of Technology, Bedford, England, 1976

Blackwell, J.A., Jr., "A Finite-Step Metod for Calculation of Theoretical Load Distributions for Arbitrary Lifting-Surface Arragements at Subsonic Speeds," TN D-5335, NASA, July 1969

Crosby, C.P., Ashman, P., Terblanche, H., "Full-Scale In-Flight Pressure Measurements on a Winglet Fitted to an AS-W 20," Technical Soaring, Volume 20, No. 3, July 1996

Eppler, R., "Induced Drag and Winglets, Technical Soaring," Volume 20, No. 3, July 1996

Fell, M.J., Spillmann, J.J., "The Effects of Wing tip devices on the performance of the Bae Jetstream,"

Jarvis, J., Selberg, B., "Investigation of Aerodynamic Improvements Using Wing Tip Sails," AIAA 99-0530, January 1999

Jupp, J., "Wing Aerodynamics and the Science of Compromise," The Aeronautical Journal, Lanchester Lecture, November 2001

Kiceniuk, T., "Dynamic Soaring and Sailplane Energetic," free flight-vol libre, Dec/Jan 2001

Lanchester, F.W., "Aerodynamics," Constable & Co, London, 1907

La Roche, U., Palffy, S., '' WING-GRID, a Novel Device for Reduction of Induced Drag on Wings,'' Proceedings ICAS 96, Sorrento, September 1996

Marsden, D.J., "Winglets for Sailplanes," Technical Soaring, Volume 15, No. 4, October 1991

Masak, P., "Winglet Design for Sailplanes," free flight-vol libre, April/May 1992

Maughmer, M.D., "The Design of Winglets for High-Performance Sailplanes," AIAA 2001-2406,

Montoya, L.C., Jacobs, P.F., Flechner, S.G., "Effect of Winglets on a First-Generation Jet Transport Wing," III- Pressure and Spanwise Load Distributions for a Semispan Model at Mach 0.3, NASA TN D-8478, June 1977

Nicks, O.W., "Wing Extension for Improving Climb Performance," AIAA-83-2556, October 1983

Nics, O.W., "A Physical View of Wing Aerodynamics," Technical Soaring, Volume 17, No. 4, October 1993

Patterson, J.C., "Wingtip Vortex Turbine," United States Patent # 4,917,332, April 17, 1991

Prandtl, L., "Theory of lifting Surfaces," NACA TN9, 1920

Smith, S., "Do Winglets Work," free flight-vol libre, Aug/Sep 1997

Snyder, M.H., "Effects of a Wingtip-Mounted propeller on Wing Lift, Induced Drag, and Shed Vortex Pattern," Aeronautical Report 68-5, Department of aeronautical Engineering, Wichita State University, December 1968

Thorsen, O.R., "Theoretical and Experimental Analysis of the Winglets designed for the High-Performance Sailplane ASW-27," Thesis, TU Delft, March 1999

Whitcomb, R.T., "A Design Approach and Selected Wind-Tunnel Result at High Subsonic Speed for Wing-Tip Mounted Winglets," NASA TN D-8260, July 1976

Volkers, D.F., Van Hengst, J., "Improving Aerodynamic Characteristics by means of Turbulence Management: A Fokker View, "The Lpswisch Book Company, 1st edition 1996